When and why does CO2 mineralization in basalts stall? A critical review of microscale passivation, pore-clogging mechanisms and the multiscale imaging needed to resolve them

Tagir Karamov[1,*], Alina Karamova[1]

[1]*Skolkovo Institute of Science and Technology (Skoltech), Moscow, Russia*

***Corresponding author:** Tagir Karamov, t.karamov@skoltech.ru

ORCID (T. Karamov): https://orcid.org/0000-0002-0413-9101

ORCID (A. Karamova): https://orcid.org/0009-0002-5910-4501

Keywords: CO_2 mineralization; basalt; carbon storage; surface passivation; pore clogging; reactive transport; multiscale imaging

Preprint statement. This manuscript is a non-peer reviewed preprint submitted to EarthArXiv. Subsequent versions of this manuscript may have slightly different content. If accepted for publication in a peer-reviewed journal, the final version will be available via the "Peer-reviewed Publication DOI" link on the EarthArXiv webpage of this preprint. Please feel free to contact the corresponding author with any feedback.

When and why does CO_2 mineralization in basalts stall? A critical review of microscale passivation, pore-clogging mechanisms and the multiscale imaging needed to resolve them

Tagir Karamov[a,*], Alina Karamova[a]

[a] *Skolkovo Institute of Science and Technology, Moscow, Russia*

[*] Corresponding author. E-mail: t.karamov@skoltech.ru

Abstract

In-situ CO_2 mineralization in basalts is among the most secure forms of geological carbon storage. Field pilots report rapid mineralization and, where monitored, stable injectivity, yet many laboratory experiments show that carbonation slows or stops long before the reactive cation inventory of the rock is consumed. We synthesise four field pilots (CarbFix1, CarbFix2, Wallula, Jizan) and 37 laboratory studies (36 experimental, one modelling) spanning 5–200 °C and 0.1–30 MPa to identify why, and to ask whether these limits apply at reservoir scale. Three microscale mechanisms are distinguished: (i) chemical isolation of olivine, glass and pyroxene by nanometre-thick Si-rich amorphous layers, which lower dissolution rates by two to more than four orders of magnitude; (ii) precipitation of smectites, zeolites and serpentine-type phases that coat pore walls, bridge micro-cracks and compete with carbonates for divalent cations; and (iii) clogging of pore throats and micro-fractures by carbonates; if all products are retained in place, carbonation increases the solid volume by 35–90%. Where both were measured, permeability and porosity were decoupled: in five of seven experiments permeability fell by up to one to two orders of magnitude for porosity losses of less than 0.2–4 percentage points — 3–60 times more than Kozeny–Carman predicts for an initial porosity of 10% — whereas in the other two permeability increased despite secondary precipitation. A Pilling–Bedworth-type volume criterion predicts that leached Si residues and calcite crusts on plagioclase are porous, so that the dense passivating layers observed on olivine require interfacial silica reprecipitation; pyrite armour proved temporary. Transport regime (Péclet and Damköhler numbers) and pore connectivity, rather than bulk porosity, decide whether reaction proceeds, passivates or clogs. Only 3 of the 37 studies imaged the reacting interface at the nanometre scale. We therefore propose a correlative workflow in which time-lapse micro-CT locates clogging and site-specific FIB-SEM/TEM resolves passivating interfaces, and formulate a research agenda for parameterising reactive-transport models of CO_2 mineralization.

Keywords: CO_2 mineralization; Carbon storage; Basalt carbonation; Reactive surface passivation; Pore clogging; Permeability evolution; Micro-CT; FIB-SEM

Abbreviations

Abbreviation	Definition
BET	Brunauer–Emmett–Teller (gas-adsorption surface area)
BIB	broad ion beam
CAMP	Central Atlantic Magmatic Province
CCUS	carbon capture, utilisation and storage
CRBG	Columbia River Basalt Group

Abbreviation	Definition
CT	computed tomography
Da	Damköhler number
DRP	digital rock physics
EDS	energy-dispersive X-ray spectroscopy
FIB	focused ion beam
ICDP	interfacial coupled dissolution–reprecipitation
k, k_0	permeability, initial permeability
LBM	lattice Boltzmann method
MORB	mid-ocean-ridge basalt
Pe	Péclet number
PNM	pore-network modelling
REV	representative elementary volume
RSA	reactive surface area
RTM	reactive-transport model
SANS	small-angle neutron scattering
$scCO_2$	supercritical CO_2
SEM	scanning electron microscopy
(S)TEM	(scanning) transmission electron microscopy
V_p/V_r	molar volume of solid products / molar volume of reactant
XRD	X-ray diffraction
ΔV_s	change in solid volume upon reaction
φ, φ_0	porosity, initial porosity

1. Introduction

Limiting global warming requires not only deep emission cuts but also the permanent removal and storage of billions of tonnes of CO_2 per year. Conventional geological storage injects supercritical CO_2 into depleted hydrocarbon fields or deep saline aquifers, where it is retained by a low-permeability caprock and, over centuries to millennia, by residual, solubility and mineral trapping [1,2]. Because mineral trapping is the slowest of these mechanisms in siliciclastic reservoirs, the long-term security of such sites depends on caprock integrity and monitoring.

Mafic and ultramafic rocks offer a fundamentally different trapping pathway. Basalts typically contain about 10 wt% CaO, 5–10 wt% MgO and about 10 wt% FeO_T, hosted in olivine, pyroxene, Ca-rich plagioclase and volcanic glass [3]. When CO_2-charged water dissolves these phases, the released divalent cations combine with dissolved inorganic carbon to precipitate calcite, magnesite, siderite and their solid solutions (ankerite, Fe-dolomite), converting CO_2 into thermodynamically stable carbonate minerals [4–7]. Basalts are among the most widespread rocks on Earth, and their theoretical storage capacity exceeds anthropogenic emissions by orders of magnitude [3,8,9]. The CarbFix pilot in Iceland demonstrated that more than 95% of the CO_2 injected as an aqueous solution was mineralised within two years [10], and the Wallula pilot in the Columbia River Basalt Group showed that supercritical CO_2 injected as a separate phase also mineralises within months to years [11,12].

These successes have shifted the scientific question from *whether* basalts can mineralise CO_2 to *how much, how fast and for how long*. Here the record is more ambiguous. Laboratory dissolution rates of olivine and basaltic glass fall by two to more than four orders of magnitude once Si-rich surface layers develop [13–15]; dissolution of Jizan basalts slowed considerably over 250 days of batch reaction [16], although in a closed reactor part of this slowdown reflects the approach to equilibrium; and core-flooding experiments report permeability losses of up to one to two orders of magnitude after porosity changes of a few tenths of a percent to about 1.5 percentage points [17–19]. In these cases, the reaction appears to be limited not by the exhaustion of reactive cations but by the progressive isolation of fresh mineral surfaces from the fluid — a phenomenon collectively termed *reactive surface passivation* — and by the loss of hydraulic access to the pore space, termed *pore clogging*. Field observations, by contrast, have not yet shown such limits: the CarbFix2 injection well retained stable injectivity over 3.5 years of continuous injection [33]. The open question is therefore not whether passivation and clogging occur, but under which conditions they will matter at reservoir scale and over decades.

Recent reviews have summarised field projects, reaction chemistry, storage capacity and modelling needs for basalt carbonation [3,20–27]. Lu et al. [21] identified the extent of passivation layers and the evolution of reactive surface area as two of the main knowledge gaps that currently prevent reactive-transport models (RTMs) from reproducing laboratory data. Akanji et al. [26] highlighted the pore-network consequences of injecting CO_2-saturated water, and Yin et al. [23] stressed the need for practical control of reaction rates. However, no review has yet focused specifically on the *microscale mechanisms* that terminate the reaction, compared them quantitatively across experimental designs, or asked which analytical methods can actually observe them.

This review addresses that gap. We (i) contrast what field pilots can and cannot tell us about passivation (Section 2); (ii) show why continuum RTMs systematically miss it (Section 3); (iii) dissect the three microscale mechanisms — Si-rich interfacial layers, secondary silicates and carbonate clogging — together with the effects of gas impurities and the conditions under which coatings fail to passivate (Section 4); (iv) synthesise 37 laboratory studies in a single comparative table and analyse it statistically (Section 5); (v) evaluate the controls exerted by thermodynamic regime, transport regime and pore topology (Section 6); and (vi) propose a correlative multiscale imaging workflow and a research agenda (Sections 7–8). Throughout, we distinguish observations from interpretations and flag where the evidence is contradictory.

2. Field-scale evidence: what pilot projects reveal and conceal

Four pilots now provide quantitative constraints on in-situ carbonation in basalt (Table 1). They differ in injection strategy, which directly shapes the fluid–rock contact and therefore the passivation and clogging risks.

Table 1. CO_2 mineralization pilots in basalt: injection strategy, reservoir conditions, mineralisation efficiency and the extent of direct microstructural evidence.

Site	Injection	Reservoir and conditions	Mineralisation	Microstructural evidence

Site	Injection	Reservoir and conditions	Mineralisation	Microstructural evidence
CarbFix1, Hellisheiði (Iceland) [10,28–32]	2012; 175 t pure CO_2 + 73 t CO_2–H_2S mixture, dissolved in water during injection	Basaltic lavas and hyaloclastites, 400–800 m; ~20–50 °C	>95% of injected CO_2 mineralised within <2 years (^{14}C, SF_6 tracer mass balance); calcite confirmed by Ca isotopes	No post-injection core; mineralisation inferred from fluid chemistry and isotopes — location of precipitates in the pore network unknown
CarbFix2, Hellisheiði (Iceland) [33,34]	2014–2017; 23,200 t CO_2 + 11,800 t H_2S (geothermal gas), dissolved in condensate	Basalt, ~750 m injection depth; >250 °C	>50% (phase 1) and >60% (phase 2) of injected C, 76–>85% of S mineralised within 4–9 months	Mass balance only; high-T secondary assemblage (carbonates, sulfides, Ca–Al silicates) competes for Ca; injectivity stable over 3.5 years [33]
Wallula Basalt Pilot (WA, USA) [11,12,35–37]	2013; 977 t supercritical CO_2 over ~3 weeks (two-phase injection)	Columbia River Basalt Group interflow zones, 830–890 m	~60% of CO_2 mineralised within 2 years (hydraulic-test inversion); injected-CO_2 origin of the nodules confirmed by C isotopes; carbonates occupy ~4% of available pore space	Chemically zoned ankerite–siderite–aragonite nodules in vesicles and vugs (micro-CT, SEM); nodule morphology depends on host-rock mineralogy
Jizan Group pilot (Saudi Arabia) [16,38,39]	2023; 131 t CO_2 co-injected with recirculated formation water (CO_2:H_2O ≈ 1:65 by mass)	Altered Oligocene–Miocene basalts, ~350 m; 45 °C; flow focused in a few wide-aperture fracture zones	70 ± 5% mineralised ~10 months after injection	Batch tests on Jizan basalts: calcite growth on grains, but dissolution rates slowed considerably with time

At **CarbFix1** (Hellisheiði, Iceland), CO_2 was dissolved in water within the injection well so that a single-phase, buoyancy-free carbonic-acid solution entered the basaltic lavas and hyaloclastites at 400–800 m depth [28–30]. Tracer mass balance using ^{14}C and SF_6 showed that over 95% of the injected carbon was mineralised within two years [10], and Ca isotopes confirmed rapid calcite precipitation [32]. The low-pH injectate dissolves the host rock near the well and the precipitation front migrates downstream as the fluid is neutralised [31,40]. The price is water: dissolved injection requires tens of tonnes of water per tonne of CO_2 [3,38].

At **CarbFix2**, a geothermal gas mixture of CO_2 and H_2S was co-injected with condensate into basalt at >250 °C. More than 50–60% of the carbon and 76–85% of the sulfur were mineralised within four to nine months [33,34]. The higher temperature accelerates basalt dissolution but also stabilises Ca-bearing silicates and sulfides that compete with carbonates for the same cations [33]. Notably, the injectivity of the injection well remained stable throughout 3.5 years of injection, indicating that host-rock permeability was not measurably affected at the well scale [33].

The **Wallula** pilot (Washington, USA) injected 977 t of supercritical CO_2 into Columbia River basalt interflow zones at 830–890 m [11,35]. Here carbonation proceeds in water films and in the formation water contacted by the buoyant CO_2 phase. Side-wall cores recovered two years later contained chemically zoned ankerite nodules in vesicles and vugs [11,36], and micro-CT of these cores quantified the nodules and pore networks in 3D [37]. Inversion of pre- and post-injection hydraulic tests indicated that approximately 60% of the CO_2 had mineralised and that the new carbonates occupied about 4% of the available pore space [12]. Wallula is thus the only pilot for which the spatial distribution of precipitates has been directly imaged —

and it shows that nodules form in vesicles and vugs, with a morphology that depends on the host mineralogy of each micro-environment [36].

The most recent pilot, in the **Jizan Group** basalts of Saudi Arabia, co-injected 131 t of CO_2 with recirculated formation water between two wells, reaching 70 ± 5% mineralisation within about ten months without importing external water [38]. Wellbore logs showed that flow is focused in a few wide-aperture fracture zones [39], and batch experiments on the same basalts recorded calcite growth on grains accompanied by a marked slowdown of dissolution with time [16].

Three conclusions follow. First, all pilots confirm rapid initial mineralisation, and at CarbFix2 injectivity remained stable over 3.5 years [33]; however, the pilots have been monitored for at most a few years and at injection rates far below the Mt yr^{-1} scale, and clogging at intermediate distances from the well (Section 6.2) would not necessarily be detected by wellhead injectivity. Second, with the partial exception of Wallula, mineralisation is quantified indirectly — by tracers, isotopes, fluid chemistry or hydraulic inversion — so *where* the carbonates precipitate within the pore network, and what happens to the residual primary-mineral surfaces, remains unobserved. Third, the pilots span a broad range of temperatures, CO_2 phase states and fracture- versus matrix-dominated flow, which means that the passivation mechanisms that matter differ from site to site. Industrial up-scaling to Mt yr^{-1} injection rates will require predictive control of these mechanisms, and that control has to come from the microscale.

3. Why continuum reactive-transport models miss passivation

Predictions of mineral trapping rely on RTMs such as TOUGHREACT, PHREEQC, CrunchFlow and related codes [41–43], which have been applied to CarbFix and Wallula [12,40,44] and, more recently, to stochastic fracture networks [45]. These codes discretise the reservoir into grid blocks that are treated as representative elementary volumes (REVs), each characterised by a single porosity, permeability and set of mineral surface areas (Fig. 1a). For a primary mineral *m*, the dissolution rate is usually written in transition-state-theory form [46–48]:

$$r_m = A_m \left[k_a(T)\, a_H^{+n} + k_n(T) \right] (1 - \Omega_m^p)^q, \qquad k_i(T) = k_{i,25} \exp[-(E_{a,i}/R)(1/T - 1/298.15)] \tag{1}$$

where A_m is the reactive surface area (RSA) per unit volume of rock, k_a and k_n are the acid and neutral rate constants, a_{H+} is the proton activity, Ω_m the saturation ratio and *p*, *q* empirical exponents. The RSA is typically initialised from BET or geometric surface areas and then updated with the mineral volume fraction, e.g.

$$A_m(t) = A_{m,0}\, [\varphi_m(t)/\varphi_{m,0}]^{2/3} \tag{2}$$

and permeability is updated from porosity by a Kozeny–Carman-type relation [49–51]:

$$k/k_0 = (\varphi/\varphi_0)^3\, [(1 - \varphi_0)/(1 - \varphi)]^2 \tag{3}$$

Equations (1)–(3) embody three assumptions that are violated by passivation. **First**, RSA is assumed to scale with the remaining volume of the primary phase. In reality, the surface that is *accessible* to the fluid is a small and variable fraction of the BET or geometric area [52–54], and a nanometre-thick Si-rich layer can reduce the effective rate by orders of magnitude while more than 90% of the mineral remains unreacted [13,14]. A model that tracks only volume fractions cannot represent this core–shell isolation. **Second**, the

rate is evaluated from the grid-averaged fluid composition, whereas precipitation is controlled by local supersaturation at mixing fronts, in dead-end fractures and in confined pores, where concentrations can differ strongly from the mean [55–57]. **Third**, Eq. (3) links permeability to the total volume of precipitate irrespective of its location. For φ_0 = 10%, a 2% loss of porosity reduces *k* by only about a factor of two (Fig. 1a). Pore-scale experiments, by contrast, show that small volumes of carbonate or clay placed in pore throats and micro-cracks reduce permeability by one to two orders of magnitude (Fig. 1b; Section 5.3) [17,18,58]. Alternative φ–k laws, such as the tubes-in-series model with a critical porosity [59], reproduce such drops only through fitted parameters that have no independent microstructural basis [51].

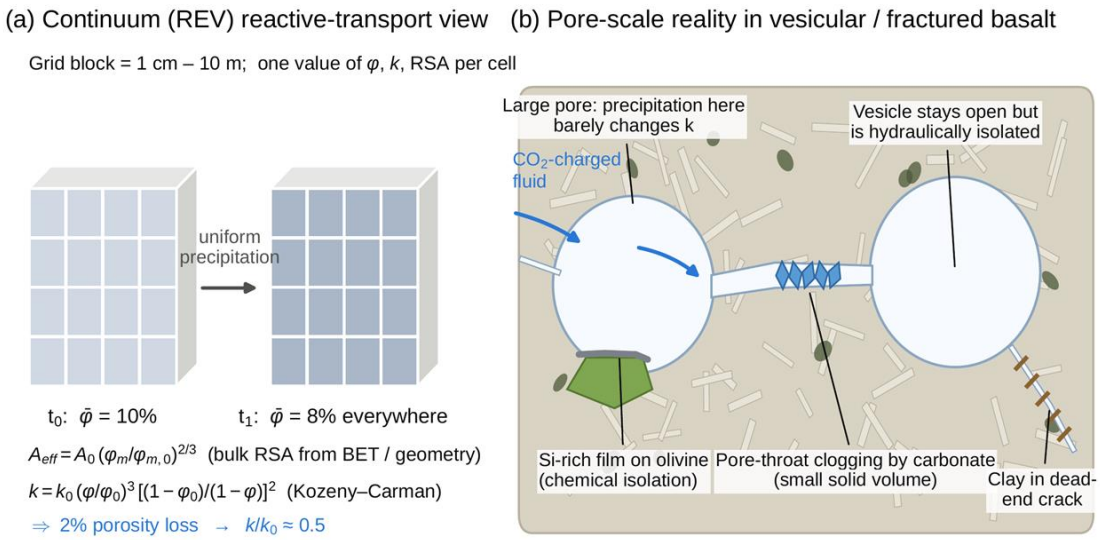

Fig. 1. Conceptual discrepancy between (a) continuum reactive-transport models, which assign one porosity, permeability and bulk reactive surface area to each grid block and assume uniform precipitation, and (b) the pore-scale reality of vesicular and fractured basalt, where a small volume of carbonate seals a hydrodynamic choke point, a Si-rich film isolates an olivine crystal, clay fills a dead-end crack and a large vesicle remains open but hydraulically disconnected. The Kozeny–Carman estimate in (a) is computed for φ_0 = 10%.

The consequence is that continuum models tend to overestimate both the rate of mineral trapping and the longevity of injectivity, and their calibration against laboratory data is often poor [21,60]. Calibrating rate constants or RSA multipliers to match one experiment does not solve the problem, because the controlling variables — coating thickness and porosity, precipitate location, throat connectivity — are not represented. Resolving these variables requires direct observation at the scale where fluid and mineral meet.

4. Microscale mechanisms of passivation and clogging

We distinguish three mechanisms that act at different length scales (Fig. 2): chemical isolation of reactive surfaces by Si-rich interfacial layers (nm), coating and bridging by secondary silicates (nm–µm), and obstruction of pore throats and fractures by carbonates (µm–mm). They are coupled: the first controls cation release, the second competes for the released cations and the third converts them into solid volume where it matters most hydraulically. We then examine gas impurities and, equally important, the evidence that coatings often do *not* passivate.

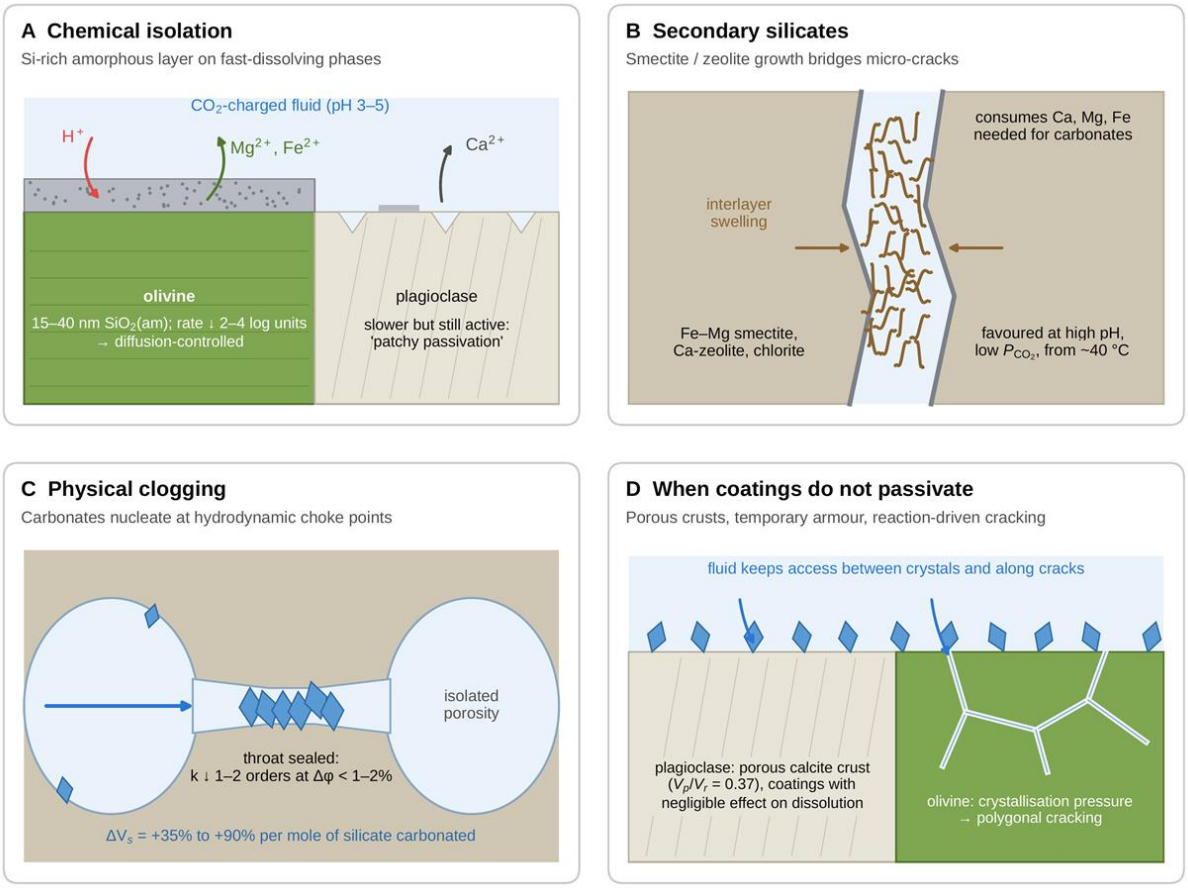

Fig. 2. Microscale mechanisms that limit CO_2 mineralization in basalt (suggested graphical abstract). (A) Chemical isolation: a 15–40 nm Si-rich amorphous layer forms on olivine (comparable layers on glass are inferred but not yet measured under storage conditions), shifting the reaction to diffusion control, whereas plagioclase remains active (patchy passivation). (B) Secondary silicates: Fe–Mg smectite, zeolite and chlorite coat walls and bridge micro-cracks, consuming the cations needed for carbonates. (C) Physical clogging: carbonate crystals nucleate in pore throats and isolate downstream porosity. (D) Conditions under which coatings do not passivate: porous carbonate crusts on plagioclase and reaction-driven cracking of olivine.

4.1. Chemical isolation by Si-rich interfacial layers

Carbonation of a basalt begins with proton-promoted dissolution of its primary phases. For forsterite, the overall reaction can be written as

$$Mg_2SiO_4 + 4\ CO_{2(aq)} + 4\ H_2O \rightarrow 2\ Mg^{2+} + 4\ HCO_3^- + H_4SiO_{4(aq)} \quad (4)$$

$$Mg^{2+} + HCO_3^- \rightarrow MgCO_3 + H^+ \quad (5)$$

with analogous reactions for fayalite, pyroxenes, Ca-plagioclase and glass. Basalt dissolution is non-stoichiometric: divalent cations are released faster than Si and Al [61–63], and the reactivity of the phases differs by orders of magnitude (Fig. 3). Under acidic conditions typical of a CO_2-charged injectate (pH 3–4), the far-from-equilibrium rates of forsterite, diopside and augite exceed that of labradorite by one to two orders of magnitude, whereas Ca-rich anorthite dissolves rapidly at low pH but becomes almost pH-independent above pH ~4.5 and is the least temperature-sensitive phase (Fig. 3) [48,64]. Basaltic glass, often the dominant reactive component of hyaloclastites, dissolves at rates comparable to or faster than olivine and releases Al as well as Si [62,65].

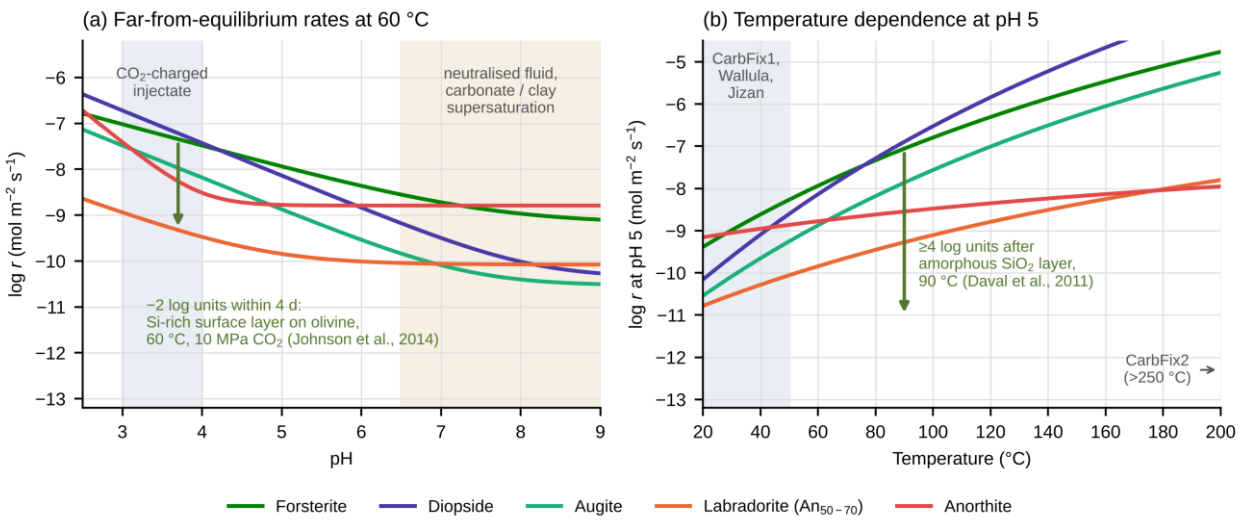

Fig. 3. Far-from-equilibrium dissolution rates of the main basalt-forming minerals computed with Eq. (1) ($\Omega \rightarrow 0$) using the acid and neutral rate parameters compiled by Palandri and Kharaka [48]: (a) as a function of pH at 60 °C; (b) as a function of temperature at pH 5. Arrows show the rate decrease measured for olivine after formation of Si-rich surface layers at 60 °C [14] and 90 °C [13]. The rates are normalised to mineral surface area and do not include the effect of coatings, which is the subject of this review. The shaded band in (b) marks the reservoir temperatures of CarbFix1, Wallula and Jizan (CarbFix2, >250 °C, lies off scale); rates above the temperature range of the underlying experiments are Arrhenius extrapolations.

Where the dissolving surface is enriched in Si relative to the bulk mineral, a residual amorphous layer develops. Two contrasting interpretations exist. In the classical *leached-layer* model, cations diffuse out of a partially depolymerised silicate framework that remains in place. In the *interfacial coupled dissolution–reprecipitation* (ICDP) model, the mineral dissolves congruently at a sharp interface and amorphous silica precipitates immediately from a thin, locally supersaturated fluid film [66–69]. The distinction is not academic: an ICDP layer can be dense and pore-poor once the interfacial fluid reaches amorphous-silica saturation, whereas a leached residue is inherently porous because the Si residue alone occupies less volume than the parent mineral (Section 4.3).

Experiments on olivine document both the formation and the kinetic consequences of these layers. Béarat et al. [15] showed at ~185 °C and ~13.5 MPa P_{CO2} that a highly defective, glassy Si-rich passivating layer inhibits olivine carbonation, and that carbonation increased markedly when particle abrasion in stirred reactors chipped this layer away. Daval et al. [13] used FIB-prepared TEM foils to characterise a ubiquitous, 15–40 nm thick, pore-poor Si-rich amorphous layer on olivine reacted at 90 °C and 20–25 MPa CO_2; long-term rates were at least four orders of magnitude lower than predicted by standard kinetic laws, and the rate was controlled by saturation with respect to amorphous silica. Johnson et al. [14] found that a Si-rich layer formed on olivine within two days at 60 °C and 10 MPa CO_2, and the dissolution rate decreased by two orders of magnitude over four days, while no more than 7 mol% of the olivine was converted to carbonate after 94 days. Passivation also operates when water is scarce: in humid supercritical CO_2 at 50 °C and 9 MPa, where reaction proceeds in thin water films — the Wallula configuration — forsterite dissolution slowed markedly after about 24 h, even far from equilibrium, because of a 2–3 nm thick Mg-depleted layer of highly polymerised amorphous silica [70]. King et al. [71] demonstrated more generally that the nature of secondary phases formed at the olivine surface decides whether carbonation continues or stalls.

Because the phases dissolve at different rates and have different Si/cation ratios, passivation in a polymineralic basalt is spatially heterogeneous — a condition we refer to as **patchy passivation** (Fig. 2A). Olivine and glass are attacked first and are the first to become shielded, whereas plagioclase, which supplies most of the Ca for calcite, continues to dissolve at a slower but steadier rate. In the Jizan experiments, plagioclase dissolution dominated cation release, but the overall dissolution rate still slowed considerably over time [16], although in these closed-system experiments the fluids rapidly approached pyroxene equilibrium and calcite saturation, so that the slowdown cannot be attributed to surface layers alone. Reactive-transport simulations built on a segmented image of reacted fractured basalt [72] show that the arrangement of minerals does not change the amount of carbonate formed but controls where it forms by setting local saturation states; the mineral mosaic at the pore wall, not only the bulk composition, therefore determines where reaction continues and where it stops.

Mechanistically, the layer shifts the rate-limiting step from surface reaction to diffusion of protons inward and cations outward. If the layer thickness δ grows and its effective diffusivity D_{eff} decreases as it densifies, the cation flux scales approximately as $D_{eff}\Delta C/\delta$, so that the rate falls with time even at constant bulk fluid chemistry. Neither δ nor D_{eff} is known for basalt-hosted phases under storage conditions, and both are accessible only to nanometre-scale methods (Section 7).

4.2. Secondary silicates: competition for cations and pore-wall coatings

As the fluid is neutralised, it becomes supersaturated not only with respect to carbonates but also to a suite of Al- and Si-bearing phases: Fe–Mg smectites (saponite, nontronite), zeolites (chabazite, stilbite, analcime), chlorite and, in olivine-rich rocks, serpentine-type minerals [21,73,74]. Their formation has two adverse consequences.

Competition for cations. Smectites and zeolites consume Ca, Mg and Fe that would otherwise form carbonates. In basaltic-glass batch experiments at 40 °C lasting up to 260 days, Fe-rich carbonates and Ca–(Mg)–Fe smectites formed together at pH < 6.5, and above pH 6.5 the solutions became supersaturated with calcite, zeolites and Mg-rich clays, which jointly controlled the availability of Ca, Mg and Fe [74]. In a 108-day large-column experiment at 50 °C and 8 MPa, no carbonate was detected in the solids although siderite was saturated; a four-day interruption of CO_2 supply raised the outlet pH to about 8, and reactive-transport modelling indicated that such pauses favour saponite and zeolite precipitation that would consume pore space [75]. Flow-through experiments at 90 °C showed that when divalent cations are limited, secondary silicates fill the pore space, whereas supplying additional Ca and Mg with seawater produced massive carbonate precipitation instead [76]. At the CarbFix site, reaction-path modelling predicts that zeolites and smectites compete with calcite as the fluid evolves [40], and at >250 °C Ca-bearing silicates become an important sink [33].

Pore-wall coatings and bridging. Unlike conformal Si-rich films, phyllosilicates grow as platy, honeycomb or fibrous aggregates projecting into the pore space. Nishiyama et al. [18] found at 200 °C that permeability decreased continuously by up to about two orders of magnitude while porosity changed by less than 1%, and identified phyllosilicate coatings that clogged pore throats downstream as the controlling factor. In fractured basalt cores flooded at 100–150 °C, high-alkalinity fluids (640 mM $NaHCO_3$) enhanced carbonation in diffusion-limited zones but also deposited clays along the advective flow paths, which the

authors considered capable of eventually obstructing flow [77]. In percolation experiments on sintered olivine at 180 °C and 12 MPa, permeability fell to 10^{-18} m^2 within 55–90 h as serpentine-type coatings formed on olivine downstream [78]. Smectites can additionally swell by interlayer hydration, the magnitude of which depends on layer charge and interlayer cation [79]; swelling allows small masses of clay to bridge micro-cracks and compartmentalise the pore network (Fig. 2B). Whether swelling at reservoir salinity and CO_2 activity is significant for basalt-hosted smectites has not been measured directly and is an open question.

4.3. Carbonate precipitation, solid-volume change and clogging

The success of carbonation is also its main hydraulic hazard: carbonation reactions increase the solid volume. Table 2 and Fig. 4 quantify this effect for the principal reactions, using standard molar volumes [80]. If all products remain where the reactant dissolved, the solid volume increases by 35% for anorthite → calcite + kaolinite and by 76–90% for olivine and pyroxene carbonation (ΔV_s in Table 2). At the reservoir scale, this expansion consumes porosity; at the pore scale, its effect depends almost entirely on *where* the solids are deposited.

Table 2. Solid-volume budget of carbonation and sulfation reactions of basalt-forming silicates (per mole of primary phase).

Primary phase	**Reaction**	**V_r**	**V carbonate / sulfate**	**V Si(–Al) phase**	**ΔV_s (%)**	**V_p/V_r carbonate only**	**V_p/V_r Si(–Al) only**
Forsterite	$Mg_2SiO_4 + 2CO_2 \rightarrow 2MgCO_3 + SiO_2(am)$	43.79	56.04	27.27	+90	1.28	0.62
Fayalite	$Fe_2SiO_4 + 2CO_2 \rightarrow 2FeCO_3 + SiO_2(am)$	46.39	58.76	27.27	+85	1.27	0.59
Enstatite	$MgSiO_3 + CO_2 \rightarrow MgCO_3 + SiO_2(am)$	31.33	28.02	27.27	+76	0.89	0.87
Diopside	$CaMgSi_2O_6 + 2CO_2 \rightarrow CaCO_3 + MgCO_3 + 2SiO_2(am)$	66.09	64.95	54.54	+81	0.98	0.83
Anorthite	$CaAl_2Si_2O_8 + CO_2 + 2H_2O \rightarrow CaCO_3 + Al_2Si_2O_5(OH)_4$	100.79	36.93	99.52	+35	0.37	0.99
Anorthite (SO_x)	$CaAl_2Si_2O_8 + H_2SO_4 + H_2O \rightarrow CaSO_4 + Al_2Si_2O_5(OH)_4$	100.79	45.94	99.52	+44	0.46	0.99
Anorthite (SO_x)	$CaAl_2Si_2O_8 + H_2SO_4 + 3H_2O \rightarrow CaSO_4{\cdot}2H_2O + Al_2Si_2O_5(OH)_4$	100.79	74.69	99.52	+73	0.74	0.99

Molar volumes (cm^3 mol^{-1}) from Robie and Hemingway [80]: forsterite 43.79, fayalite 46.39, enstatite 31.33, diopside 66.09, anorthite 100.79, magnesite 28.02, siderite 29.38, calcite 36.93, SiO_2 glass (proxy for amorphous silica) 27.27, kaolinite 99.52, anhydrite 45.94, gypsum 74.69. $V_p/V_r > 1$ is the Pilling–Bedworth–Velbel condition for a potentially continuous, protective layer [81].

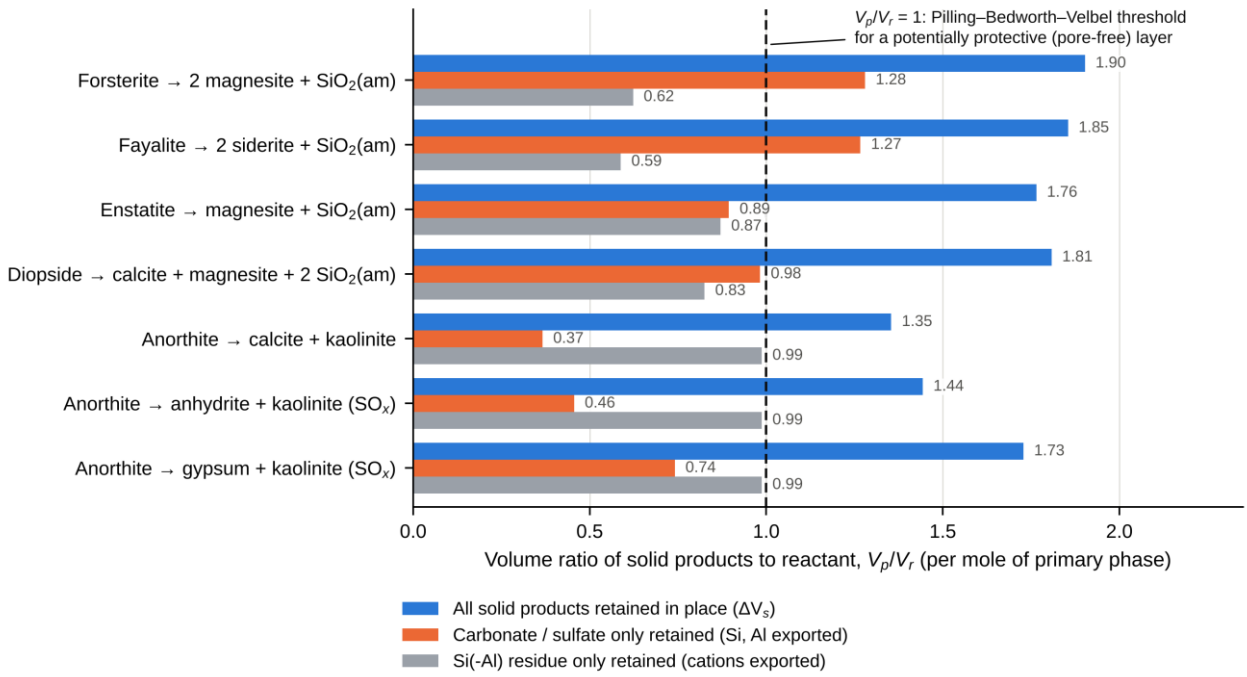

Fig. 4. Solid-volume budget of carbonation and sulfation reactions per mole of primary silicate, calculated from molar volumes in Table 2. Blue: all products retained in place (ΔV_s). Orange: only the carbonate (or sulfate) retained, Si and Al exported. Grey: only the Si(–Al) residue retained, cations exported. The dashed line marks V_p/V_r = 1, the Pilling–Bedworth–Velbel threshold above which a surface layer can be continuous and pore-free [81].

Precipitation in large vesicles, as observed in the Wallula cores [11,36,37], consumes storage volume but barely affects permeability. Precipitation in pore throats and micro-cracks, by contrast, disconnects whole clusters of porosity (Fig. 1b, Fig. 2C). Several factors favour throat-localised precipitation: fluid mixing and neutralisation are fastest where flow converges; reactive surfaces exposed in micro-cracks have the highest surface-to-volume ratio; and diffusion-limited dead ends allow supersaturation to build up [77,82]. In fractured basalt cores, precipitates filled 5.4% and 15% of the fracture volume after up to 40 weeks at 100 and 150 °C, respectively [83], and carbonate precipitation was maximal 10–25 mm from the open end of dead-end fractures [82]. In core-flooding experiments on fractured basalt, carbonate and clay precipitation reduced the fracture volume by 35% at 100 °C and 48% at 150 °C over 10–12 days, with carbonate bridging that increased with distance into dead-end fractures [77]. Time-lapse X-ray CT of mixing-induced precipitation in cracked basalt showed carbonate nucleating on pore walls and in the micro-cracks that connect larger pores; permeability fell by one to two orders of magnitude within hours, whereas porosity declined by less than 4% over 24–90 h [58]. In naturally fractured basalt at 40 °C, $CaCO_3$ accumulated at the fracture outlet and in transverse fractures, reducing permeability from 30.65 to about 2.5 mD (−92%) while porosity decreased by less than 0.2% [17]; part of this decline, however, was attributed to migration of fine particles and dissolution of fracture asperities rather than to precipitation.

Pore size itself modulates precipitation. Solubility and nucleation barriers depend on pore size and surface chemistry, so that precipitation can be suppressed in nanopores and favoured in larger pores, or vice versa, depending on the substrate [84–86]. In vesicular basaltic glass flooded with CO_2-acidified seawater at 80 °C, precipitation was nucleation-limited and became visible only after the flow rate was reduced tenfold [87]. These observations imply that the timing and location of the first nuclei, which no continuum model resolves, largely determine the subsequent permeability evolution.

The volume budget also offers a simple, testable criterion for **when a coating can be protective**. By analogy with the Pilling–Bedworth rule for metal oxidation, Velbel [81] argued that a surface layer can be continuous and pore-free only if the volume of product exceeds that of the reactant consumed ($V_p/V_r > 1$). Applying this criterion to carbonation (Fig. 4, Table 2) yields three insights. (i) A pure leached Si residue on olivine or pyroxene has V_p/V_r = 0.59–0.87 and should therefore be porous; the dense, passivating layers observed experimentally [13] require additional silica *reprecipitation* from the interfacial fluid, i.e. an ICDP-type mechanism at or near SiO_2(am) saturation. (ii) Magnesite or siderite retained on olivine or fayalite gives $V_p/V_r \approx 1.3$, so carbonate rims on these phases can in principle armour the grain. (iii) Calcite retained on plagioclase gives $V_p/V_r = 0.37$; calcite crusts on Ca-plagioclase are expected to be discontinuous and porous, in agreement with experiments showing that calcite coatings have negligible effects on silicate dissolution rates [88]; earlier companion studies addressed the same question for basaltic glass and diopside [89,90]. The criterion ignores interfacial energies and crystal habit, but it rationalises why passivation is phase-specific and why the same carbonate may be harmless on one substrate and protective on another. Strictly, the criterion applies to layers formed in place from the components of the reactant; carbonate overgrowths nucleated from solution need not obey it, and calcite precipitated on olivine and enstatite also failed to slow their dissolution [88].

Finally, the volume increase can generate stresses large enough to fracture the reacting rock. Reaction-driven cracking has been predicted theoretically [91–93] and observed in olivine carbonation experiments as polygonal cracking and dissolution channels imaged by synchrotron micro-CT [94,95]. In dunite deformed under CO_2-rich fluids, precipitate layers along fractures acted as compliant 'proppants' while permeability nevertheless declined log-linearly [96]. Whether such self-sustaining fracturing occurs in basalts under realistic effective stresses, and whether it can outpace clogging, is unresolved.

4.4. Co-injected impurities

Industrial CO_2 streams and geothermal gases contain H_2S, SO_x, NO_x and O_2. Their effects on passivation are mixed. In batch experiments with 1% H_2S at 90 °C and 10 MPa, pyrite coatings formed before carbonates, but this armouring proved temporary over 3.5 years and carbonation subsequently proceeded [97]; at CarbFix2, sulfur was mineralised as efficiently as carbon [33,34], and co-mineralisation of carbon and sulfur has been proposed as a general strategy for geothermal reservoirs [98]. With 1 wt% SO_2 and 1 wt% O_2 in $scCO_2$, gypsum blades and natrojarosite–natroalunite spherules nucleated first and served as templates for later phases, and carbonation was delayed [99]. Sulfates are hydraulically more consequential than calcite: per mole of Ca, anhydrite (45.9 cm^3) and gypsum (74.7 cm^3) occupy 24% and 102% more volume than calcite (36.9 cm^3) [80], and the V_p/V_r of gypsum retained on anorthite (0.74) is double that of calcite (Table 2). The lower pH generated by SO_x may delay Si-layer formation, but faster and bulkier sulfate precipitation is likely to dominate the clogging risk; this trade-off has not been tested in flow-through experiments.

4.5. When coatings do not passivate: reconciling contradictory evidence

Passivation is not universal, and a credible model must explain the negative results as well as the positive ones. Rosenbauer et al. [100] reacted MORB, tholeiite and picrite with CO_2-charged brine at 50–200

°C and 30 MPa for up to 4400 h and observed no grain armouring even after repeated CO_2 additions; uptake reached 8–26 wt% CO_2, with a maximum at 100 °C. Stockmann et al. [88] precipitated calcite on olivine, enstatite, augite, labradorite, basaltic glass and peridotite and found that the coatings negligibly affected silicate dissolution, although earlier mixed-flow experiments had interpreted carbonate precipitates as blocking reactive surfaces [101]. Pyrite armouring was temporary [97], serpentine mesh textures in peridotite enhanced rather than inhibited fluid infiltration [102], and reaction-driven cracking continuously generated new porosity in olivine aggregates [94,95].

These results are compatible with the mechanisms in Sections 4.1–4.3 once three conditions are considered. (1) **Layer density**: only layers with $V_p/V_r > 1$ or with reprecipitated, pore-poor silica passivate; porous carbonate crusts do not. (2) **Fluid saturation state**: Si-rich layers become protective near SiO_2(am) saturation, which is reached quickly in batch reactors with high surface-area-to-volume ratios [13] and, in flow-through systems, mainly in preferential, fast-flow zones and at high flow rates, where the fastest-dissolving phases are attacked first [17,103]. (3) **Mechanical feedback**: crystallisation pressure and differential volume change can crack coatings and grains. Passivation is therefore a *conditional* outcome determined by the coupled chemistry, transport and mechanics of each micro-environment — which explains why bulk experiments with different designs reach opposite conclusions.

5. Synthesis of laboratory evidence

5.1. Scope and structure of the compilation

Table 3 compiles 37 laboratory studies that report secondary mineralogy, passivation or permeability changes during basalt– or olivine–CO_2–water interaction, together with the field pilots in Table 1. For each study we list the material, experimental set-up, temperature, pressure or P_{CO2}, fluid, duration, secondary phases, quantified petrophysical changes, the dominant mechanism(s) according to the classification of Section 4, and the diagnostic methods used. Set-ups are grouped as batch (closed reactors), mixed-flow (stirred, open powder reactors) and flow-through (core, column or percolation) experiments. One entry (#23) is a reactive-transport model of flow-through experiments; it is listed because it isolates the effect of transport, but it is excluded from the statistics in Fig. 5. Mechanism codes are: SL — Si-rich interfacial layer; SS — secondary silicates; CC — carbonate precipitation or clogging; IM — impurity-derived (S-bearing) phases; NP — no measurable passivation or dissolution-dominated behaviour; RC — reaction-driven cracking. Peridotite and olivine-aggregate experiments are included because they isolate the most reactive component of basalt and provide most of the nanoscale evidence. Values marked ‡ are taken from the compilation of Lu et al. [21] where the primary paper does not state them explicitly.

Table 3. Synthesis of laboratory studies of basalt– and olivine–CO_2–water interaction: conditions, secondary phases, petrophysical changes and the dominant passivation/clogging mechanisms.

#	Ref.	Material	Set-up; fluid	T (°C)	P (MPa)	Duration	Secondary phases	Δk, Δφ, rate	Mech.	Diagnostics	Key observation
A. Interfacial layers, carbonate coatings and whole-rock batch reactivity											
1	[15]	Olivine powder	Stirred autoclave (batch); 1 M NaCl + 0.64 M $NaHCO_3$	~185	~13.5 (P_{CO2})	—†	Magnesite; Si-rich amorphous rims	—	SL	SEM, TEM	Defective, glassy Si-rich layer inhibits carbonation; abrasion that chips the layer enhances carbonation
2	[13]	San Carlos olivine powder	Batch (Teflon capsules; Dickson autoclave); H_2O–CO_2	90	20–25 ($scCO_2$)	1–45 d	Amorphous SiO_2 layer (15–40 nm)	Rates ≥4 log units below model	SL	FIB-TEM, STEM-EDXS	Dense (pore-poor) layer once SiO_2(am) saturation is reached
3	[14]	Olivine (Fo_{92})	Batch; H_2O / 0.5 M NaCl	60	10 (P_{CO2})	≤94 d	Si-rich layer, SiO_2(am), magnesite	Rate ↓ 2 log units in 4 d	SL	SEM, solution chemistry	Layer forms within 2 d; ≤7 mol% olivine carbonated
4	[70]	Forsterite	In-situ high-pressure IR cell, humid $scCO_2$ (thin H_2O film); Adsorbed/thin water film	50	9 ($scCO_2$)	3 h – 5 d	2–3 nm Mg-depleted, highly polymerised amorphous SiO_2 layer; Mg-carbonate	Dissolution slows after ~24 h	SL	In-situ IR, ^{29}Si MAS NMR, TEM-EDS	Passivation far from equilibrium in water-limited (Wallula-type, two-phase) conditions
5	[101]	Diopside; basaltic glass	Mixed-flow reactor; pH 8.2 solution	70	—	45–60 d	Calcite	—	CC	Solution chemistry, SEM	Carbonate precipitates interpreted to block reactive surfaces (early evidence)
6	[88]	Olivine, enstatite, augite, labradorite, basaltic glass, peridotite seeds	Mixed-flow reactor; Calcite-supersaturated solutions	25	—	~10 and ~70 d	Calcite coatings (extensive on olivine/enstatite; minimal on glass)	—	NP	SEM	Calcite coatings negligibly affect silicate dissolution — porous carbonate crusts are not passivating
7	[100]	MORB, tholeiite, picrite	Batch (flexible-cell); CO_2-charged brine	50–200	30	≤4400 h	Ferroan magnesite; SiO_2(am)	8–26 wt% CO_2 uptake	NP	XRD, SEM	Maximum rate at 100 °C; no grain armouring after repeated CO_2 injections
8	[61]	Crystalline basalt (Stapafell)	Mixed-flow reactor; pH 2–11 solutions	5–75	—	steady state	—	—	NP	Solution chemistry	Baseline kinetics: non-stoichiometric (incongruent) element release; olivine/glass > pyroxene > plagioclase reactivity
9	[16]	Jizan Group basalts (375–665 m)	Closed batch; Na_2CO_3/$NaHCO_3$ solutions	60	—	≤250 d	Calcite; no Al-bearing secondary phases detected	—	CC	SEM-EDS, solution chemistry	Plagioclase-dominated dissolution slowed considerably over time in a closed system (approach to equilibrium contributes); flow-through operation recommended
B. Basaltic glass, seawater and secondary silicates											
10	[74]	Basaltic glass (Stapafell)	Batch; CO_2-charged water	40	P_{CO2} ≈0.1–1.3 (24–305 mmol kg^{-1} CO_2)	≤260 d	Ca–Mg–Fe carbonates; Ca–(Mg)–Fe smectites; Fe-(oxy)hydroxides	—	SS/CC	SEM-EDS, EPMA	Clays and carbonates compete for Ca, Mg, Fe; at pH > 6.5 calcite, zeolites and Mg-clays become supersaturated

#	Ref.	Material	Set-up; fluid	T (°C)	P (MPa)	Duration	Secondary phases	Δk, Δφ, rate	Mech.	Diagnostics	Key observation
11	[60]	Basaltic glass	High-pressure column (2.3 m flow path); Pure vs CO_2-charged water (0.3 M CO_2)	22, 50	P_{CO2} ≤2.2	37–104 d	Fe-bearing secondary phases; carbonates only on outlet degassing	—	SS	Solution chemistry, SEM	pH 3.4 → 4.5 only; fluid supersaturated with clays and Fe/Al hydroxides; models mispredicted outlet chemistry
12	[75]	Basaltic glass	Large column reactor (flow); CO_2-charged water (20 mM CO_2, P_{CO2} ≈0.06 MPa); 4-day CO_2 interruption	50	8	108 d (66 d reported)	No carbonate detected in solids (siderite saturated); modelled Fe/Mg-saponite, allophane, moganite	—	SS	XRD, SEM, RTM	CO_2 interruption raised pH to ~8 → saponite/zeolite stability; such pauses would consume pore space (modelled)
13	[21,76]	Basaltic glass; crystalline basalt	Flow-through reactor; NH_4HCO_3 solutions vs CO_2-charged synthetic seawater, neutral pH	90	P_{CO2} 0.4–4 ‡	4.6–68 d ‡	Smectites/zeolites, Fe-oxides, NH_4-dawsonite (cation-poor); calcite, magnesite (seawater)	Pore space lost to silicates when Ca, Mg depleted	SS/CC	SEM-EDS, XRD	Cation supply decides between silicate and carbonate pore filling; risk of clogging near the well with seawater
14	[104]	MORB glass	Batch; CO_2-charged seawater	130	0.25 and 1.6 (P_{CO2})	7 months	Calcite, aragonite, siderite, ankerite (low P_{CO2}); magnesite (high P_{CO2})	~20% of CO_2 mineralised in 5 months	CC	XRD, SEM	Seawater supplies extra Ca/Mg; P_{CO2} selects carbonate phase
15	[105]	Basalt, basanite cores (Auckland VF)	Batch; Rock-equilibrated water + CO_2	100	5.5	140 d	Ankerite; zeolite; phyllosilicates	Porosity ↑ (dissolution dominant)	NP/SS	SEM, ultrasonics	Precipitation highest in glass-rich, porous samples
16	[106]	Basalt cores (Idaho)	Batch reactor; Basalt-equilibrated water + CO_2 (3.5 mol L^{-1})	100	8.3	30 weeks	Carbonates in fractures and compliant pores	k ↓ ≤1 order; φ ↓ 2–3%	CC	Ultrasonics, thin sections	V_P ↑ 4–20%; compliant-pore filling dominates elastic and hydraulic response
C. Flood-basalt series and gas impurities											
17	[21,107]	Flood basalts (CRBG, CAMP, Deccan, Karoo)	Static batch; CO_2-saturated water (± 1.5% H_2S)	100 ‡	10.3 ‡	≤854 d ‡ (H_2S series 181 d)	Fe-rich globular carbonates; calcite; zoned Ca/Fe carbonates	—	CC	SEM, XRD	Similar bulk chemistry, strongly different carbonation rates and morphologies
18	[108]	CRBG, CAMP basalts	Batch ($scCO_2$ and aqueous phases); Wet $scCO_2$ / CO_2-saturated water	34–116	7.4–25.5	30–180 d	Aragonite, calcite, ankerite nodules; kutnohorite-like phases	—	CC	SEM, XRD	Reactivity rises with depth-equivalent P–T; faster carbonation in wet $scCO_2$
19	[97]	Five flood basalts	Batch; $scCO_2$-saturated water + 1% H_2S	90	10	≤3.5 yr	Pyrite coatings, then cation-substituted carbonates	—	IM	SEM, XRD	Pyrite armouring precedes carbonation but proved temporary
20	[99]	Five basalts	Batch; Water + $scCO_2$ with 1 wt% SO_2 + 1 wt% O_2	90	10	48 and 98 d	Gypsum blades; natrojarosite–natroalunite spherules; onset of carbonation	—	IM	XRD, TGA, SEM	Sulfate/jarosite phases nucleate first and template later minerals
D. Fractures, cores and permeability evolution											
21	[83]	Flood and serpentinised basalt, engineered fractures	Static batch; Water equilibrated with CO_2	100, 150	10	≤40 weeks	Siderite, Mg–Ca–Fe carbonates	Precipitates fill 5.4% (100 °C) and 15% (150 °C) of fracture volume	CC	SEM-EDS, Raman	Carbonation detectable after 6 weeks; RTM predicts siderite after ~1 d

#	Ref.	Material	Set-up; fluid	T (°C)	P (MPa)	Duration	Secondary phases	Δk, Δφ, rate	Mech.	Diagnostics	Key observation
22	[82]	Unaltered and serpentinised basalt, grooved fractures	Flow-through (120 h) vs batch (6 weeks); CO_2-saturated water	45, 100	10	120 h / 6 weeks	Mg-bearing siderite (batch only)	—	CC	SEM-EDS, Raman	Advective flow → net dissolution; diffusion-limited dead ends → carbonate maximum 10–25 mm from fracture mouth
23	[72]	Fractured basalt (segmented reacted core)	2D reactive-transport model (CrunchTope) of flow-through experiments; CO_2-acidified fluid; 9 flow conditions	100	10	simulated ≤10 yr	Calcite, magnesite, siderite (modelled)	—	CC	Segmented SEM image + RTM	Diffusion sustains reactions longer and yields more carbonate than advection; mineral mosaic controls where, not how much
24	[77]	Fractured basalt cores (main path + dead-end fractures)	Core flooding; 6.3 or 640 mM $NaHCO_3$ equilibrated with CO_2	100, 150	10	10–12 d	Carbonates localised on cation-supplying grains; clays in advective paths; carbonate bridges in dead ends	Fracture volume ↓ 35% (100 °C), 48% (150 °C)	CC/SS	X-ray CT, SEM-EDS, Raman, 2D RTM	High alkalinity boosts carbonation in diffusion-limited zones, but clays filling flow paths could obstruct injection
25	[109]	Naturally porous (vesicular) basalt	Static batch; CO_2-saturated water	100	10	20 weeks	Carbonates in fracture network	~1.24 kg CO_2 m^{-3} yr^{-1}	CC	Micro-CT, SEM	Projected filling of accessible pores in ~40 yr
26	[110,111]	Intact basalt cores	Core flooding; 1 M NaCl, P_{CO2} 12.5 MPa, pH 3.3; 0.1 vs 0.01 mL min^{-1}	150	15 (pore), 20 (confining)	0.5–32.8 d	Al–Si secondary phases; siderite	k ↑ (>10× in one core) at high Q; k ↓ slightly at low Q	NP/SS	X-ray CT, SANS, SEM	Flow rate and initial pore structure, not initial k, controlled the outcome
27	[19]	Basalt cores (7 samples)	Exposure + permeametry; CO_2-rich seawater	~21	1.5 (pore), 5 (confining)	28–110 d	Carbonates (from fluid chemistry)	k ↓ up to 1 order (3/7 samples); macro-φ ↓ ≤1.5%	CC	Micro-CT (50 µm), PNM	Fit requires up to 43% loss of sub-50-µm microporosity — clogging hides below CT resolution
28	[18]	Basalt cores (200 mm long)	Flow-through, constant ΔP (3 runs); CO_2-saturated water; 0.0003–0.7 mL min^{-1}	200	10 (pore); P_{CO2} ≈10	15–21 d	Phyllosilicate coatings downstream	k ↓ to 1.2–2.6% of k_0; φ change <1%	SS	X-ray CT, SEM-EDS	Pore-throat clogging by phyllosilicate coatings controls permeability loss
29	[17]	Naturally fractured basalt	Reactive percolation; CO_2–water; 0.1 then 0.01 mL min^{-1}	40	4 (back), 10 (confining)	192 h	$CaCO_3$ at fracture outlet and transverse fractures; Si-rich layers at the higher flow rate	k: 30.65 → ~2.5 mD (−92%); φ ↓ <0.2%	CC/SL	CT, SEM-EDS	Lower flow rate drove an additional 83% permeability loss; fines migration contributed at the higher rate
30	[58]	Thermally cracked Icelandic basalt cores	Flow-through, mixing-induced precipitation (two-fluid co-injection); Ca- and carbonate-bearing solutions	~23 (ambient)	0.34 (inlet), ΔP 0.24	24–90 h	Carbonate nucleating on pore walls and in micro-cracks linking larger pores	k ↓ 1–2 orders within hours; φ ↓ <4%	CC	Time-lapse X-ray CT, ultrasonics	Flow and precipitation continued after the permeability drop
31	[87]	Vesicular basaltic glass (3 facies)	Flow-through; CO_2-acidified seawater, pH 5.4–5.5	80	~1	30 d	Calcite, smectite-like coatings, amorphous $CaCO_3$	No significant k change; modal coordination number = 2	CC	Micro-CT (5 µm), SEM-EDS, PNM	Nucleation-limited; precipitation only at 0.005 mL min^{-1}; serial connectivity → high clogging vulnerability

#	Ref.	Material	Set-up; fluid	T (°C)	P (MPa)	Duration	Secondary phases	Δk, Δφ, rate	Mech.	Diagnostics	Key observation
32	[112]	Basalt cores (Ø 5 cm)	Flow-through, two-fluid co-injection; 1 M $CaCl_2$ + 1 M Na_2CO_3; 0.142 or 0.035 mL min^{-1} per inlet	24	~0.6 (confining); outlet atmospheric	hours (in-situ imaging); CT after 6 months	Calcite	—	CC	4D neutron + X-ray imaging (ILL, PSI, ESRF)	Steady transverse mixing vs fluctuating mixing caused by trapped air; late calcite from diffusive mixing
E. Olivine-rich and ultramafic analogues											
33	[103,113]	Sintered dunite	Reactive percolation; 0.6 M $NaHCO_3$ + CO_2	160	12 (P_{CO2} 9.5)	—†	Magnetite + Si-rich layer (preferential-flow zones); magnesite, siderite, Mg-phyllosilicates (reduced-flow zones)	φ decreases only where diffusion dominates	SL/CC	X-ray microtomography, SEM	Si-rich layer inhibits olivine dissolution in fast-flow zones; moderate injection rates sustain carbonation and permeability
34	[78]	Sintered olivine (± basalt)	Reactive percolation; $NaHCO_3$–CO_2 water; 1 vs 0.1 mL h^{-1}	180	12	55–90 h	Ca–Mg carbonates; serpentine-type coatings on olivine (downstream)	k → 10^{-18} m^2 in 55–90 h	SS/CC	Solution chemistry, SEM	Hydration competes with carbonation; flow rate controls both
35	[102]	Partially serpentinised / weathered peridotite	Batch; NaCl or $CaCl_2$ solutions	200	13–18 (P_{CO2})	15–25 d	Magnesite (NaCl); calcite ($CaCl_2$)	—	NP	SEM, EMP	Serpentine mesh not reactive but improved fluid infiltration
36	[96]	Dunite (thermally cracked)	Triaxial / hydrostatic flow; DI water; 0.6–1.5 M $NaHCO_3$	23, 150	10 (pore), 15 (confining)	3–7 d	Magnesite, calcite, lizardite, brucite along fractures	Log-linear k decline; steeper with CO_2	CC/SS	SEM	Precipitate layers act as compliant 'proppants', reducing stiffness and strength
37	[94,95]	Sintered olivine aggregate cups + olivine sand	In-situ synchrotron imaging cell; $NaHCO_3$ solution	200	10 (pore), 13 (confining)	30–140 h	Magnesite; serpentine	Porosity generated	RC	Synchrotron 3D/4D micro-CT	Polygonal cracks after ~65 h; non-uniform expansion and dissolution channels keep fresh surface accessible

Mechanism codes: SL — Si-rich interfacial layer; SS — secondary silicates (smectite, zeolite, chlorite, serpentine-type); CC — carbonate precipitation / clogging; IM — impurity-derived (S-bearing) phases; NP — no measurable passivation or dissolution-dominated; RC — reaction-driven cracking / porosity generation. P is total or confining/pore pressure unless P_{CO2} is indicated. ‡ — value taken from the compilation of Lu et al. [21] (Table B1); † — not stated in the accessible abstract or open full text; see the original paper. k — permeability; φ — porosity; Q — flow rate; VF — volcanic field.

5.2. P–T coverage and experimental design

Figure 5a plots the 41 P–T conditions for which both values were reported. Three biases are apparent. First, experiments cluster at 90–150 °C and 10–15 MPa — a window chosen for fast kinetics rather than for representativeness — whereas the operating pilots span ~20–50 °C (CarbFix1, Wallula, Jizan) and >250 °C (CarbFix2). Second, low-temperature (<60 °C) flow-through experiments, which are most relevant to shallow, water-saturated injection, are scarce. Third, only 3 studies addressed gas impurities (one as an H_2S sub-series), and none of them in a flow-through configuration.

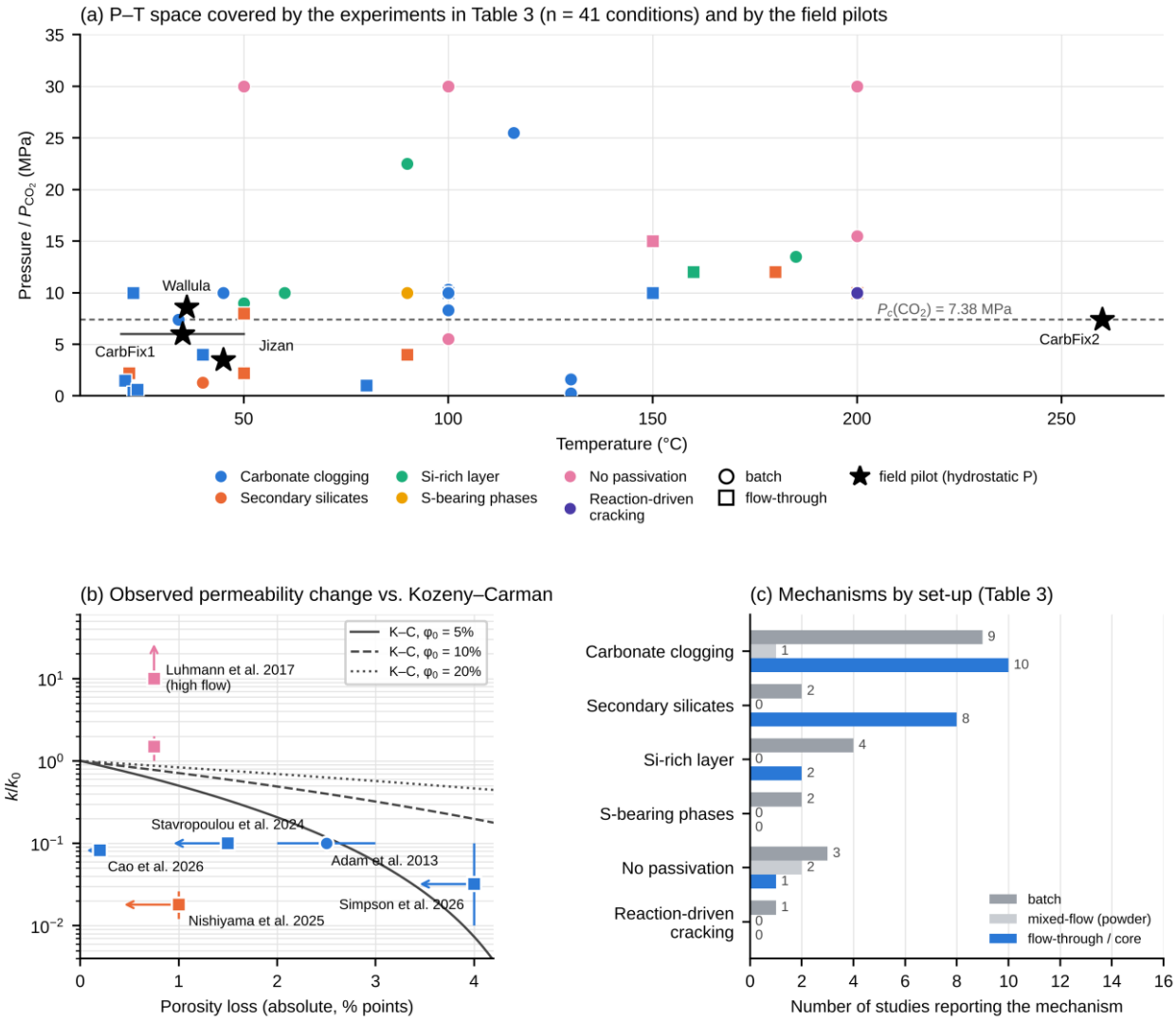

Fig. 5. Quantitative synthesis of Table 3. (a) Temperature–pressure conditions of the experiments (colour: dominant mechanism; symbol: set-up) and of the field pilots (stars; pressure estimated as hydrostatic from injection depth). (b) Permeability ratio k/k_0 versus absolute porosity loss for experiments that report both quantities; arrows indicate upper bounds on porosity loss; vertical bars show ranges of k/k_0 and the upward arrow a lower bound. Luhmann et al. [110]: high-flow cores, porosity loss from X-ray CT of the larger pores ((U)SANS porosity increased); their low-flow cores (slight k decrease) and Kanakiya et al. [105] (k and porosity increased) are not plotted because no numerical values are reported. Curves are Kozeny–Carman predictions (Eq. 3) for initial porosities of 5, 10 and 20%. (c) Frequency of mechanisms reported in batch, mixed-flow and flow-through/core experiments (row 23, a model, excluded) (studies with several mechanisms are counted once per mechanism).

5.3. Permeability is decoupled from porosity

The most consistent quantitative result of the compilation is the decoupling of permeability from porosity (Fig. 5b). In five of the seven experiments that report both quantities, permeability fell by up to one to two orders of magnitude while porosity decreased by less than 0.2–4 percentage points [17–19,58,106]: by about one order of magnitude in naturally fractured basalt [17], seawater-exposed cores [19] and Idaho basalt [106], and by up to two orders of magnitude at 200 °C [18] and during mixing-induced precipitation [58]. The decoupling also operates in the opposite direction: at high flow rates, basalt cores at 150 °C gained permeability (by more than an order of magnitude in one core) although X-ray CT showed a net 0.7–0.8% loss of larger-pore porosity [110], and Auckland basalts gained both porosity and permeability despite ankerite and aluminosilicate precipitation [105]. For φ_0 = 5–20%, Eq. (3) predicts $k/k_0 \approx 0.5$–0.85 for a 1% porosity loss; for φ_0 = 10% the observed values are 3–60 times lower than predicted, the discrepancy being largest where the porosity change is smallest, whereas for a low initial porosity (5%) and the larger porosity losses [58,106] Eq. (3) comes within a factor of about two of the observations. Pore-network modelling of the basalt experiments of Stavropoulou et al. [19] required up to a 43% reduction of the sub-50-µm microporosity — invisible at the 50 µm CT resolution — to reproduce the measured permeability loss. Nooraiepour et al. [87] measured a modal pore coordination number of only 2 in vesicular basalts, compared with 4–6 in sandstones, and concluded that serial connectivity makes such rocks inherently vulnerable to permeability impairment by modest, distributed precipitation. Together, these data indicate that Kozeny–Carman-type laws are structurally inappropriate for carbonating basalts and that φ–k relations must be derived from the connectivity and throat-size distribution of the specific rock.

5.4. Mechanisms differ between batch and flow-through experiments

Figure 5c shows that Si-rich interfacial layers were identified mostly in batch experiments (4 of 6 studies), whereas secondary-silicate coatings and carbonate clogging dominate in flow-through and core experiments. This pattern is not merely a sampling artefact: batch reactors with high surface-area-to-volume ratios reach SiO_2(am) saturation quickly and therefore favour dense interfacial layers [13], whereas flow-through systems export Si and Al and concentrate precipitation where the fluid is neutralised. The flow rate is a key control within flow experiments: in basalt cores at 150 °C, permeability increased at 0.1 mL min^{-1} but decreased at 0.01 mL min^{-1} [110,111]; in fractured basalt, reducing the rate from 0.1 to 0.01 mL min^{-1} caused an additional 83% permeability loss [17]; and in grooved fractures, advective flow produced net dissolution while diffusion-limited dead ends hosted siderite [82]. In percolated sintered dunite, preferential-flow zones developed magnetite and a Si-rich layer that inhibited olivine dissolution, whereas reduced-flow zones hosted magnesite, siderite and Mg-phyllosilicates, and porosity decreased only where diffusion dominated [103]; serpentine-type coatings controlled the permeability collapse of percolated olivine at 180 °C [78].

5.5. The observational gap

Of the 37 studies, 11 used X-ray or neutron tomography, but only 3 imaged the reacting mineral–fluid interface at the nanometre scale (TEM or FIB-TEM), and all of these were performed on olivine powders rather than on basalt. No study has yet combined time-lapse micro-CT localisation of clogging with site-

specific FIB-SEM or TEM of the same interfaces in basalt. The thickness, porosity and composition of passivating layers on basaltic glass, pyroxene and plagioclase under storage conditions — the parameters needed to replace Eq. (2) — are therefore unknown. This is the central gap addressed in Section 7.

6. Controls exerted by thermodynamic regime, transport regime and pore topology

6.1. Temperature, pH, P_{CO2} and fluid chemistry

Temperature accelerates both dissolution and precipitation (Fig. 3b), but not equally. Activation energies for olivine and pyroxene dissolution (~67–96 kJ mol^{-1} for the acid mechanism) exceed those of plagioclase (~17–42 kJ mol^{-1}) [48], so heating increases the contrast between fast- and slow-dissolving phases and thus the degree of patchy passivation. Carbonate precipitation kinetics also rise steeply with temperature [114,115], and the maximum extent of basalt carbonation in batch experiments occurred at about 100 °C [100]. At higher temperatures and lower P_{CO2}, smectites, zeolites, chlorite and Ca–Al silicates become increasingly competitive [33,73], and at 200 °C phyllosilicate coatings controlled permeability loss [18]. Reactivity of flood basalts in the presence of $scCO_2$ increased with depth-equivalent P–T, from limited carbonation at 7.4 MPa and 34 °C to extensive ankerite nodules at 25.5 MPa and 116 °C [108]. The 'optimal' window is therefore a compromise between fast cation release and avoidance of non-carbonate sinks, and the threshold at which the balance tips toward clogging is site-specific.

The pH trajectory is the second master variable. The injectate (pH 3–4) dissolves primary phases near the well; as cations are released, the pH rises and supersaturation develops downstream [31]. In column experiments with CO_2-charged water, the pH rose only from 3.4 to 4.5 and carbonates did not precipitate inside the column [60], whereas an interruption of CO_2 supply raised the pH to about 8 and, according to reactive-transport modelling, shifted the system toward clay and zeolite stability [75]. P_{CO2} selects the carbonate phase: at 130 °C, calcite, aragonite, siderite and ankerite formed at ~0.25 MPa P_{CO2} but magnesite formed exclusively at ~1.6 MPa [104]. Finally, cation supply matters: CO_2-charged seawater reacts with mafic rocks at higher rates than fresh water at the same pH [65,116] and favours carbonates over silicates [76,104], but it also increases the volume of precipitate per unit of pore fluid and therefore the clogging risk [19,87].

6.2. Transport regime: Péclet and Damköhler numbers

The outcomes compiled in Section 5 can be organised by two dimensionless numbers (Fig. 6a): the Péclet number, $Pe = uL/D$, which compares advective and diffusive transport over a characteristic length L, and the Damköhler number, $Da = k_rL/u$, which compares reaction and advection rates (in diffusion-dominated zones, where $u \rightarrow 0$, the relevant measure is the second Damköhler number, $Da_{II} = k_rL^2/D$). In advection-dominated, low-Da conditions, the fluid remains undersaturated and dissolution prevails, with stable or increasing permeability. In advection-dominated, high-Da conditions, reaction fronts develop and precipitation is localised where the fluid first neutralises, often in throats and at fracture outlets. Under diffusion-limited conditions ($Pe < 1$) — dead-end fractures, the rock matrix and poorly connected vesicle clusters — supersaturation builds up, carbonates and amorphous silica accumulate, and passivation and sealing of the entrances dominate [72,77,82]. Most flow-rate series in Table 3 move from the first toward the second or third regime as the rate decreases; an exception is the 200 °C series of [18], in which the rate of

permeability loss was almost independent of flow rate. Because injection rates decline with distance from the well, a single injection creates all three regimes in sequence, which suggests — as a hypothesis still to be tested — that clogging is most likely not at the wellbore but at intermediate distances where the fluid is neutralised in poorly connected pore space; this would be consistent with the stable wellhead injectivity at CarbFix2 [33].

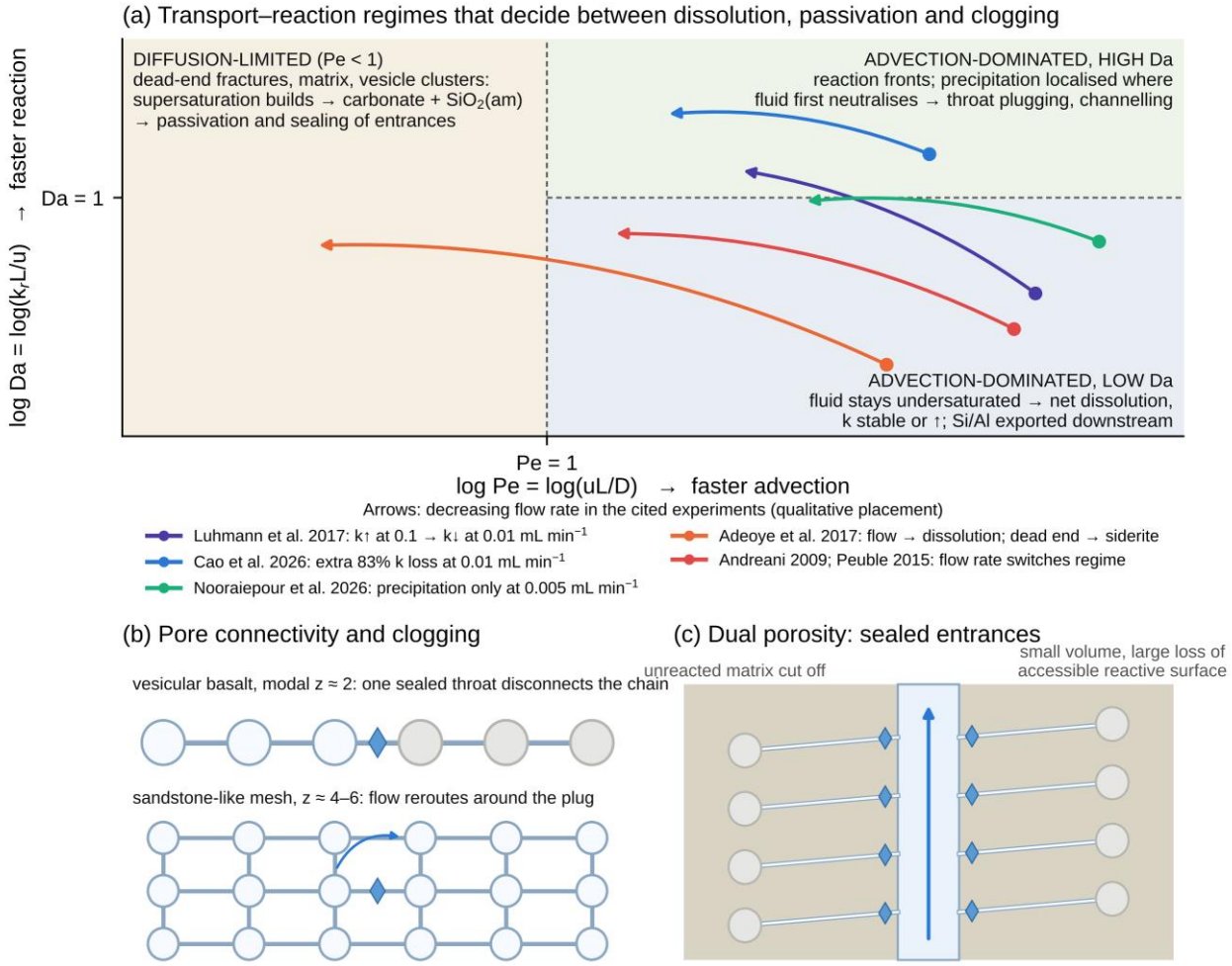

Fig. 6. (a) Transport–reaction regimes defined by the Péclet (Pe) and Damköhler (Da) numbers, with the direction of change observed in flow-rate series of Table 3 (qualitative placement). (b) Effect of pore connectivity: in vesicular basalt with a modal coordination number z ≈ 2 [87], one sealed throat disconnects the chain, whereas in a meshed network (z ≈ 4–6) flow reroutes. (c) Dual porosity: precipitation at the entrances of micro-cracks and matrix pores isolates a large reactive surface with a small volume of solid.

6.3. Pore topology and dual porosity

Basalts are dual- or multi-porosity media: large vesicles and cooling joints are connected by narrow micro-cracks, inter-crystal pores and altered glass. Fluid flow and advective mass transfer follow the few highest-conductivity paths — at Jizan, three wide-aperture fracture zones [39] — and stochastic modelling identifies fracture-network connectivity as the primary control on mineralisation efficiency [45]. Two topological features make basalts particularly sensitive to clogging (Fig. 6b, c). First, low coordination numbers mean that the network has little redundancy: a sealed throat disconnects all downstream pores [87]. Second, the entrances of micro-cracks and matrix pores branching off the main pathways are diffusion-limited zones in which precipitation is favoured [77,82]; sealing these entrances isolates a large fraction of

the reactive surface with a very small volume of solid. Evaluating the clogging risk of a candidate formation therefore requires a shift from 'how much pore space is available' to 'how the pore space is connected', i.e. from porosity to topology. Comparable non-linear and non-monotonic permeability responses to fluid–rock reaction and thermal exposure have been documented in organic-rich shales and carbonate reservoirs using the same combination of CT, NMR and ion-milling microscopy [117–120], which supports the transferability of these imaging workflows to basalts.

7. Bridging the gap: a correlative multiscale imaging workflow

7.1. Limits of conventional characterisation

Bulk methods (XRD, XRF, thermogravimetry, effluent chemistry, BET) quantify how much carbonate formed and how fast cations were released, but provide no spatial context (Table 4). They cannot distinguish a carbonate that filled a vesicle harmlessly from one that sealed a throat, and they are blind to amorphous silica. Conventional SEM-EDS of reacted surfaces shows only the outermost precipitates and hides the underlying interface; mechanical polishing of thin sections plucks clays and destroys nanometre-thick leached or reprecipitated layers. Effluent mass balance also suffers from the 'multi-source, multi-sink' problem of polymineralic systems [21].

Table 4. Analytical methods for passivation and clogging studies: resolution, information content and limitations.

Method	Resolution / field of view	Information on passivation and clogging	Limitations	Refs.
XRD (Rietveld), XRF, TGA	Bulk; LOD ~0.5–2 wt%	Identity and amount of carbonates, clays, zeolites	No spatial context; amorphous SiO_2 and poorly ordered clays under-detected	[21]
Effluent chemistry, mass balance	Reactor scale	Dissolution rates, saturation states, extent of carbonation	Multi-source/multi-sink ambiguity; cannot locate sinks	[21,60]
BET gas adsorption	Bulk specific surface	Initial surface area for RSA	Overestimates accessible RSA; crushing destroys texture	[52–54]
SEM-EDS on polished sections	~10 nm–1 µm; mm–cm field	Coating morphology, phase maps	2D; polishing plucks clays and damages nm-thick layers	[121]
BIB-SEM	nm imaging over ~1–2 mm^2 cross-sections	Artefact-poor large-area sections of coatings and throats; statistics	2D; site selection must be guided by 3D data	[121–123]
Laboratory X-ray micro-CT	~0.5–50 µm voxel; mm–cm field	3D pore network; precipitate location before/after reaction; DRP input	Sub-voxel films and microporosity invisible; weak carbonate/basalt contrast	[19,37,124,125]
Synchrotron 4D CT; neutron imaging	~0.3–2 µm; seconds–minutes	In-situ dynamics of dissolution, precipitation, cracking; neutrons sensitive to H (water, clays)	Beam-time access; small samples	[94,112,126,127]
FIB-SEM serial sectioning	~3–20 nm voxel; 10–50 µm field	3D geometry and porosity of coatings; throat closure; layer continuity	Small field — needs CT targeting; Ga implantation, curtaining, beam damage of hydrous phases	[128–131]
FIB-TEM, STEM-EDS/EELS	<1 nm	Layer thickness, composition gradients, crystallinity, sharp vs diffuse interfaces (ICDP vs leaching)	~10 × 5 µm lamellae; limited statistics	[13,66,67]
SANS, NMR	Bulk, nm–µm pore sizes	Evolution of surface area and micro-/nanoporosity	Indirect; model-dependent inversion	[110,118]
DRP: PNM, LBM, direct Navier–Stokes	Voxel-based	Δk from imaged precipitates; rock-specific φ–k laws; upscaled reaction rates	Segmentation sensitivity; REV size	[55,57,132,133]

7.2. Non-destructive 3D localisation by X-ray micro-CT and digital rock physics

X-ray micro-CT resolves the pore network of a core plug at voxel sizes of ~0.5–50 μm without altering it [124,125]. Scanning the same sample before and after (or during) reaction, registering the volumes and subtracting them localises dissolution and precipitation relative to the original pore bodies and throats [57,126,127,134]. In basalt, this approach has located carbonate nodules in Wallula cores [37], precipitates in engineered and natural fractures [17,77,109] and carbonate in micro-cracks during mixing-induced precipitation [58]; time-lapse neutron and synchrotron imaging further resolve the dynamics of mixing fronts [112]. Segmented images are the input for digital rock physics: pore-network models and lattice-Boltzmann or Navier–Stokes solvers compute permeability directly from the imaged geometry, replacing Eq. (3) with a rock-specific φ–k relation [55,132,133]. The limitation is resolution. Si-rich films, clay coatings and the sub-50-μm microporosity that controls permeability in some basalts [19] lie below the voxel size, and partial-volume effects make thin carbonate rims difficult to segment from the basalt matrix.

7.3. Site-specific nanoscale analysis by FIB-SEM and TEM

Dual-beam FIB-SEM removes material with a focused Ga^+ or Xe^+ plasma ion beam, exposing pristine cross-sections at a site chosen from the CT data, and can acquire serial-section 3D volumes with voxel sizes of a few nanometres [128–131]. It can cut through the carbonate crust, the clay coating and the Si-rich layer into the unreacted primary phase, measuring the thickness, continuity, internal porosity and composition of each layer, and it can extract electron-transparent lamellae for (S)TEM-EDS/EELS analysis of the interface at sub-nanometre resolution, as done for olivine [13] and feldspar [66,67]. Broad-ion-beam (BIB) polishing complements FIB by providing artefact-poor cross-sections over mm^2 areas for statistical analysis of coatings and pore throats [121,122]. These ion-milling and correlative imaging methods are mature in shale and carbonate petrophysics, where they have been combined with CT and NMR to quantify the alteration of mineral matrix, organic matter and pore structure under thermal and thermobaric exposure [118,123,135]; transferring them to reactive mafic systems is technically straightforward. Specific precautions for basalt carbonation include low-dose imaging of hydrous phases (smectite, amorphous silica), protective Pt or C caps, use of plasma FIB to avoid Ga implantation in Fe-rich phases, and correlative registration of FIB sites within the CT volume.

7.4. Proposed workflow

We propose the following correlative workflow (Fig. 7), designed to deliver the parameters that current RTMs lack:

1. Characterise the pristine core (petrography, XRD, porosity, k_0) and acquire a baseline micro-CT volume at the highest resolution compatible with a representative volume (in practice, a whole-plug scan at ~10–25 μm complemented by sub-plugs 2–5 mm across at ≤2 μm).
2. React the core under controlled P–T and flow conditions spanning at least two Péclet regimes, recording permeability and effluent chemistry continuously.

3. Re-image the same core, register the volumes and map precipitates relative to pore bodies, throats and dead ends; compute k from the images by DRP and compare with measured k(t).
4. Select interfaces from the CT data — olivine, glass, pyroxene and plagioclase walls in throats, bodies and dead ends — and analyse them by FIB-SEM tomography and FIB-TEM.
5. Translate the measurements into model parameters: layer thickness and effective diffusivity per phase (replacing Eq. 2), coverage fractions of carbonate and clay coatings, and a rock-specific φ–k law (replacing Eq. 3).
6. Validate the parameterised RTM by predicting k(t) and CO_2 uptake of an independent core before the experiment is run.

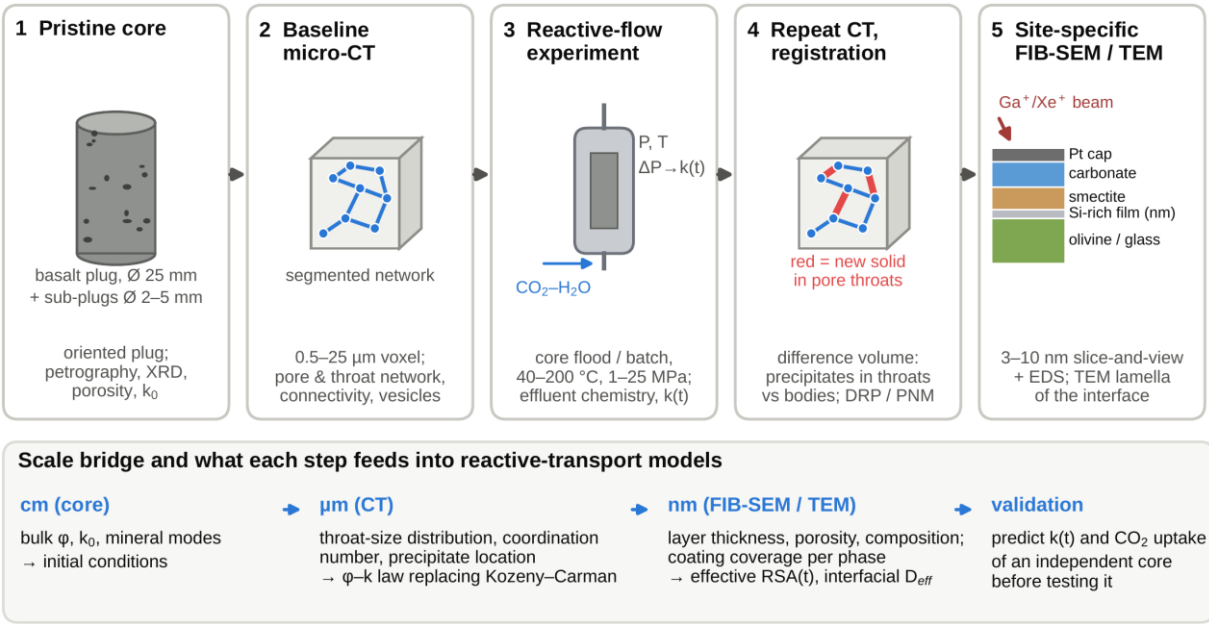

Fig. 7. Proposed correlative workflow linking core-scale experiments, micro-CT localisation of clogging and site-specific FIB-SEM/TEM analysis of passivating interfaces, and the model parameters delivered at each scale. Panel 5 is schematic.

8. Research agenda

Table 5 summarises the main open questions identified in this review, each formulated as a testable hypothesis together with the approach required to test it. Three priorities stand out. First, the conditions under which Si-rich layers become dense and passivating in polyphase basalts (rather than in olivine powders) must be established, with explicit comparison of batch and flow-through designs. Second, the location of the first carbonate and clay nuclei relative to pore throats must be measured in 4D and translated into φ–k laws that account for connectivity. Third, experiments should move closer to operating conditions: low-temperature, water-saturated flow at realistic rates; intermittent injection; seawater and recirculated formation water; and industrial gas impurities. Wherever possible, experiments should be run on cores from operating pilots (CarbFix, Wallula, Jizan), whose field performance provides an independent test of the up-scaled predictions.

Table 5. Research agenda: open questions, testable hypotheses and recommended approaches.

Knowledge gap	Why it matters	Testable hypothesis	Recommended approach
Conditions for dense, passivating Si-rich layers in polyphase basalt	Controls the 2–4 order rate drop; unknown for glass, pyroxene, plagioclase	Layers become passivating only where the interfacial fluid reaches SiO_2(am) saturation; at Pe > 1 they remain porous	Paired batch/flow-through tests on the same basalt; FIB-TEM of each phase; Si isotopes
Coverage and porosity of carbonate crusts per substrate	Decides whether carbonation self-limits	Crusts are protective only where V_p/V_r > 1 (olivine, fayalite), not on plagioclase	FIB-SEM tomography of crust porosity; tracer diffusion through crusts
Location of first nucleation (throats vs bodies vs dead ends)	Governs permeability loss per unit precipitate	Nuclei form preferentially in micro-cracks and dead ends where supersaturation builds	Time-lapse micro-CT/neutron imaging with registration; PNM
Rock-specific φ–k relations	Kozeny–Carman under-predicts k loss by 10–100×	k/k_0 follows a percolation-type law controlled by coordination number and throat-size distribution	DRP on 4D CT data; PNM calibrated on measured k(t)
Clay–zeolite vs carbonate competition during realistic operation	Non-carbonate sinks consume cations and pore space	Injection pauses and pH excursions switch precipitation to smectite/zeolite	Column/core tests with intermittent CO_2; XRD + TEM of coatings
Impurities (H_2S, SO_x, O_2) under flow	Industrial streams are impure	Sulfate phases precipitate first and clog faster than carbonates	Flow-through tests with impurity-bearing CO_2; FIB-SEM of templates
Mechanical feedback: cracking vs sealing	Could sustain reactivity	Reaction-driven cracking requires low effective stress and fast reaction	Triaxial flow tests with synchrotron CT; acoustic emission
Up-scaling from cores to pilots	Design of Mt-scale injection	Microscale parameters predict field k(t) and mineralisation	Imaging of cores from CarbFix, Wallula and Jizan; blind prediction of field data

9. Conclusions

1. Passivation and clogging, not cation exhaustion, limit carbonation in many laboratory systems. Field pilots show rapid initial mineralisation and, at CarbFix2, stable injectivity over 3.5 years, but laboratory data show that olivine dissolution can fall by two to more than four orders of magnitude after Si-rich layers form, and that permeability can collapse while most of the reactive inventory remains. Whether these limits operate at reservoir scale and over decades remains to be shown.

2. Three coupled microscale mechanisms operate at different scales: nanometre-thick Si-rich interfacial layers that isolate fast-dissolving phases (patchy passivation); secondary silicates that coat pore walls, bridge micro-cracks and compete for cations; and carbonates (and sulfates, when impurities are present) that obstruct pore throats and fractures.

3. Permeability is decoupled from porosity, in both directions. In five of seven compiled experiments that report both, k decreased by up to one to two orders of magnitude for porosity losses below ~0.2–4 percentage points — 3–60 times more than Kozeny–Carman predicts for φ_0 = 10%; in the other two, k increased despite secondary precipitation. Pore connectivity, not bulk porosity, governs injectivity in vesicular and fractured basalt.

4. Passivation is conditional. A Pilling–Bedworth–Velbel volume criterion, the Si saturation state of the interfacial fluid and mechanical feedback (reaction-driven cracking) together help explain why dense Si-rich layers can passivate olivine whereas calcite crusts on plagioclase do not, and why batch and flow-through experiments reach different conclusions.

5. The decisive parameters are unmeasured in basalts. Only a few studies imaged the reacting interface at the nanometre scale, all on olivine powders. A correlative workflow combining time-lapse micro-CT, digital rock physics and site-specific FIB-SEM/TEM can deliver layer thicknesses, coating coverage and rock-specific φ–k laws, which are required to turn reactive-transport models into predictive design tools for industrial CO_2 mineralization.

Acknowledgments

This research was supported by the Russian Science Foundation, grant No. 26-77-00091, https://rscf.ru/project/26-77-00091/.

References

[1] IPCC, IPCC Special Report on Carbon Dioxide Capture and Storage, B. Metz, O. Davidson, H.C. de Coninck, M. Loos, L.A. Meyer (Eds.), Cambridge University Press, Cambridge, 2005.

[2] S.M. Benson, D.R. Cole, CO_2 sequestration in deep sedimentary formations, Elements 4 (2008) 325–331. https://doi.org/10.2113/gselements.4.5.325

[3] S.Ó. Snæbjörnsdóttir, B. Sigfússon, C. Marieni, D. Goldberg, S.R. Gislason, E.H. Oelkers, Carbon dioxide storage through mineral carbonation, Nat. Rev. Earth Environ. 1 (2020) 90–102. https://doi.org/10.1038/s43017-019-0011-8

[4] E.H. Oelkers, S.R. Gislason, J. Matter, Mineral carbonation of CO_2, Elements 4 (2008) 333–337. https://doi.org/10.2113/gselements.4.5.333

[5] P.B. Kelemen, J. Matter, In situ carbonation of peridotite for CO_2 storage, Proc. Natl. Acad. Sci. U.S.A. 105 (2008) 17295–17300. https://doi.org/10.1073/pnas.0805794105

[6] J.M. Matter, P.B. Kelemen, Permanent storage of carbon dioxide in geological reservoirs by mineral carbonation, Nat. Geosci. 2 (2009) 837–841. https://doi.org/10.1038/ngeo683

[7] S.R. Gislason, E.H. Oelkers, Carbon storage in basalt, Science 344 (2014) 373–374. https://doi.org/10.1126/science.1250828

[8] B.P. McGrail, H.T. Schaef, A.M. Ho, Y.-J. Chien, J.J. Dooley, C.L. Davidson, Potential for carbon dioxide sequestration in flood basalts, J. Geophys. Res. Solid Earth 111 (2006) B12201. https://doi.org/10.1029/2005JB004169

[9] P. Kelemen, S.M. Benson, H. Pilorgé, P. Psarras, J. Wilcox, An overview of the status and challenges of CO_2 storage in minerals and geological formations, Front. Clim. 1 (2019) 9. https://doi.org/10.3389/fclim.2019.00009

[10] J.M. Matter, M. Stute, S.Ó. Snæbjörnsdóttir, E.H. Oelkers, S.R. Gislason, E.S. Aradottir, B. Sigfusson, I. Gunnarsson, H. Sigurdardottir, E. Gunnlaugsson, G. Axelsson, H.A. Alfredsson, D. Wolff-Boenisch, K. Mesfin, D. Fernandez de la Reguera Taya, J. Hall, K. Dideriksen, W.S. Broecker, Rapid carbon mineralization for permanent disposal of anthropogenic carbon dioxide emissions, Science 352 (2016) 1312–1314. https://doi.org/10.1126/science.aad8132

[11] B.P. McGrail, H.T. Schaef, F.A. Spane, J.B. Cliff, O. Qafoku, J.A. Horner, C.J. Thompson, A.T. Owen, C.E. Sullivan, Field validation of supercritical CO_2 reactivity with basalts, Environ. Sci. Technol. Lett. 4 (2017) 6–10. https://doi.org/10.1021/acs.estlett.6b00387

[12] S.K. White, F.A. Spane, H.T. Schaef, Q. Miller, M.D. White, J.A. Horner, B.P. McGrail, Quantification of CO_2 mineralization at the Wallula basalt pilot project, Environ. Sci. Technol. 54 (2020) 14609–14616. https://doi.org/10.1021/acs.est.0c05142

[13] D. Daval, O. Sissmann, N. Menguy, G.D. Saldi, F. Guyot, I. Martinez, J. Corvisier, B. Garcia, I. Machouk, K.G. Knauss, R. Hellmann, Influence of amorphous silica layer formation on the dissolution rate of olivine at 90 °C and elevated pCO_2, Chem. Geol. 284 (2011) 193–209. https://doi.org/10.1016/j.chemgeo.2011.02.021

[14] N.C. Johnson, B. Thomas, K. Maher, R.J. Rosenbauer, D. Bird, G.E. Brown Jr., Olivine dissolution and carbonation under conditions relevant for in situ carbon storage, Chem. Geol. 373 (2014) 93–105. https://doi.org/10.1016/j.chemgeo.2014.02.026

[15] H. Béarat, M.J. McKelvy, A.V.G. Chizmeshya, D. Gormley, R. Nunez, R.W. Carpenter, K. Squires, G.H. Wolf, Carbon sequestration via aqueous olivine mineral carbonation: Role of passivating layer formation, Environ. Sci. Technol. 40 (2006) 4802–4808. https://doi.org/10.1021/es0523340

[16] A. Omar, M. Addassi, D. Berno, A. Alqahtani, N. Menegoni, S. Arkadakskiy, J. Fedorik, Z. Ahmed, N. Kunnummal, S.R. Gislason, T. Finkbeiner, A. Afifi, H. Hoteit, E.H. Oelkers, An experimental study of the mineral carbonation potential of the Jizan Group basalts, Int. J. Greenh. Gas Control 141 (2025) 104323. https://doi.org/10.1016/j.ijggc.2025.104323

[17] X. Cao, L. Xu, P. Li, G. Xie, X. Li, Q. Li, Mineralization and permeability evolution of naturally-fractured basalt: Insights from CO_2–water–rock reactive-percolation experiments, J. Rock Mech. Geotech. Eng. 18 (2026) 5046–5056. https://doi.org/10.1016/j.jrmge.2025.10.024

[18] N. Nishiyama, M. Sorai, K. Masuoka, M. Shiga, Changes in permeability and pore structure induced by CO_2–water–basalt interaction: Insights from flow-through experiments at 200 °C, J. Geophys. Res. Solid Earth 130 (2025) e2025JB031141. https://doi.org/10.1029/2025JB031141

[19] E. Stavropoulou, C. Griner, L. Laloui, Impact of CO_2-rich seawater injection on the flow properties of basalts, Int. J. Greenh. Gas Control 134 (2024) 104128. https://doi.org/10.1016/j.ijggc.2024.104128

[20] A. Raza, G. Glatz, R. Gholami, M. Mahmoud, S. Alafnan, Carbon mineralization and geological storage of CO_2 in basalt: Mechanisms and technical challenges, Earth-Sci. Rev. 229 (2022) 104036. https://doi.org/10.1016/j.earscirev.2022.104036

[21] P. Lu, J. Apps, G. Zhang, A. Gysi, C. Zhu, Knowledge gaps and research needs for modeling CO_2 mineralization in the basalt–CO_2–water system: A review of laboratory experiments, Earth-Sci. Rev. 254 (2024) 104813. https://doi.org/10.1016/j.earscirev.2024.104813

[22] X. Cao, Q. Li, L. Xu, Y. Tan, A review of in situ carbon mineralization in basalt, J. Rock Mech. Geotech. Eng. 16 (2024) 1467–1485. https://doi.org/10.1016/j.jrmge.2023.11.010

[23] Y. Yin, L. Zhang, X. Cao, Q. Li, M. Gan, Y. Wang, Progress, challenges, and prospects of CO_2 mineral sequestration in basalt: A critical review, Appl. Energy 381 (2025) 125127. https://doi.org/10.1016/j.apenergy.2024.125127

[24] M. Wang, X. Dai, S. Sang, S. Liu, S. Zheng, W. Zhou, Z. Zhengyan, Y. Qiu, X. Song, X. Shi, Y. Song, G. Feng, V. Vandeginste, CO_2 mineralization projects, techniques, mechanisms, potential and future outlook in basalt: A review, Renew. Sustain. Energy Rev. 221 (2025) 115920. https://doi.org/10.1016/j.rser.2025.115920

[25] E.A. Owusu, J. Wu, E.A. Appiah, W.A. Marfo, N. Yuan, X. Ge, K. Ling, S. Wang, Carbon mineralization in basaltic rocks: Mechanisms, applications, and prospects for permanent CO_2 sequestration, Energies 18 (2025) 3489. https://doi.org/10.3390/en18133489

[26] S.P. Akanji, L. Esteban, A. Giwelli, J. Sarout, A. Keshavarz, S. Iglauer, In-situ carbon mineralization through injection of CO_2-saturated water into basalts: Effects on pore network, Adv. Colloid Interface Sci. 348 (2026) 103710. https://doi.org/10.1016/j.cis.2025.103710

[27] M.H. Rasool, M. Ahmad, Reactivity of basaltic minerals for CO_2 sequestration via in situ mineralization: A review, Minerals 13 (2023) 1154. https://doi.org/10.3390/min13091154

[28] S.R. Gislason, D. Wolff-Boenisch, A. Stefansson, E.H. Oelkers, E. Gunnlaugsson, H. Sigurdardottir, B. Sigfusson, W.S. Broecker, J.M. Matter, M. Stute, G. Axelsson, T. Fridriksson, Mineral sequestration of carbon dioxide in basalt: A pre-injection overview of the CarbFix project, Int. J. Greenh. Gas Control 4 (2010) 537–545. https://doi.org/10.1016/j.ijggc.2009.11.013

[29] B. Sigfusson, S.R. Gislason, J.M. Matter, M. Stute, E. Gunnlaugsson, I. Gunnarsson, E.S. Aradottir, H. Sigurdardottir, K. Mesfin, H.A. Alfredsson, D. Wolff-Boenisch, M.T. Arnarsson, E.H. Oelkers, Solving the carbon-dioxide buoyancy challenge: The design and field testing of a dissolved CO_2 injection system, Int. J. Greenh. Gas Control 37 (2015) 213–219. https://doi.org/10.1016/j.ijggc.2015.02.022

[30] H.A. Alfredsson, E.H. Oelkers, B.S. Hardarsson, H. Franzson, E. Gunnlaugsson, S.R. Gislason, The geology and water chemistry of the Hellisheidi, SW-Iceland carbon storage site, Int. J. Greenh. Gas Control 12 (2013) 399–418. https://doi.org/10.1016/j.ijggc.2012.11.019

[31] S.Ó. Snæbjörnsdóttir, E.H. Oelkers, K. Mesfin, E.S. Aradóttir, K. Dideriksen, I. Gunnarsson, E. Gunnlaugsson, J.M. Matter, M. Stute, S.R. Gislason, The chemistry and saturation states of subsurface fluids during the in situ mineralisation of CO_2 and H_2S at the CarbFix site in SW-Iceland, Int. J. Greenh. Gas Control 58 (2017) 87–102. https://doi.org/10.1016/j.ijggc.2017.01.007

[32] P.A.E. Pogge von Strandmann, K.W. Burton, S.O. Snæbjörnsdóttir, B. Sigfússon, E.S. Aradóttir, I. Gunnarsson, H.A. Alfredsson, K.G. Mesfin, E.H. Oelkers, S.R. Gislason, Rapid CO_2 mineralisation into calcite at the CarbFix storage site quantified using calcium isotopes, Nat. Commun. 10 (2019) 1983. https://doi.org/10.1038/s41467-019-10003-8

[33] D.E. Clark, E.H. Oelkers, I. Gunnarsson, B. Sigfússon, S.Ó. Snæbjörnsdóttir, E.S. Aradóttir, S.R. Gíslason, CarbFix2: CO_2 and H_2S mineralization during 3.5 years of continuous injection into basaltic rocks at more than 250 °C, Geochim. Cosmochim. Acta 279 (2020) 45–66. https://doi.org/10.1016/j.gca.2020.03.039

[34] I. Gunnarsson, E.S. Aradóttir, E.H. Oelkers, D.E. Clark, M.Þ. Arnarson, B. Sigfússon, S.Ó. Snæbjörnsdóttir, J.M. Matter, M. Stute, B.M. Júlíusson, S.R. Gíslason, The rapid and cost-effective capture and subsurface mineral storage of carbon and sulfur at the CarbFix2 site, Int. J. Greenh. Gas Control 79 (2018) 117–126. https://doi.org/10.1016/j.ijggc.2018.08.014

[35] B.P. McGrail, H.T. Schaef, F.A. Spane, J.A. Horner, A.T. Owen, J.B. Cliff, O. Qafoku, et al., Wallula basalt pilot demonstration project: Post-injection results and conclusions, Energy Procedia 114 (2017) 5783–5790. https://doi.org/10.1016/j.egypro.2017.03.1716

[36] C.T. Depp, Q. Miller, J. Crum, J.A. Horner, H.T. Schaef, Pore-scale microenvironments control anthropogenic carbon mineralization outcomes in basalt, ACS Earth Space Chem. 6 (2022) 2836–2847. https://doi.org/10.1021/acsearthspacechem.2c00165

[37] A. Battu, Q. Miller, R. Cao, A.T. Owen, H.T. Schaef, 3D quantification of pore networks and anthropogenic carbon mineralization in stacked basalt reservoirs, Environ. Sci. Technol. 58 (2024) 3747–3754. https://doi.org/10.1021/acs.est.3c06163

[38] E.H. Oelkers, S. Arkadakskiy, Z. Ahmed, N. Kunnummal, J. Fedorik, M. Marchesi, M. Addassi, A. Omar, N. Menegoni, S.R. Gislason, G. Bjornsson, D. Berno, T. Finkbeiner, A. Afifi, H. Hoteit, CO_2 subsurface mineral storage by its co-injection with recirculating water, Nature 651 (2026) 954–958. https://doi.org/10.1038/s41586-026-10130-5

[39] N. Menegoni, J. Fedorik, Y. Panara, D. Berno, M. Addassi, A. Omar, E. Oelkers, A. Afifi, H. Hoteit, S. Arkadakskiy, N. Kunnummal, Z. Ahmed, S.R. Gíslason, G. Bjornsson, T. Finkbeiner, Subsurface fracture network characterization for a CO_2 basalt mineralization target: New insight on fluid flow from wellbore logs for the Jizan Group, Geoenergy 3 (2025). https://doi.org/10.1144/geoenergy2024-037

[40] S.Ó. Snæbjörnsdóttir, S.R. Gislason, I.M. Galeczka, E.H. Oelkers, Reaction path modelling of in-situ mineralisation of CO_2 at the CarbFix site at Hellisheidi, SW-Iceland, Geochim. Cosmochim. Acta 220 (2018) 348–366. https://doi.org/10.1016/j.gca.2017.09.053

[41] T. Xu, N. Spycher, E. Sonnenthal, G. Zhang, L. Zheng, K. Pruess, TOUGHREACT Version 2.0: A simulator for subsurface reactive transport under non-isothermal multiphase flow conditions, Comput. Geosci. 37 (2011) 763–774. https://doi.org/10.1016/j.cageo.2010.10.007

[42] D.L. Parkhurst, C.A.J. Appelo, Description of input and examples for PHREEQC version 3 — A computer program for speciation, batch-reaction, one-dimensional transport, and inverse geochemical calculations, U.S. Geological Survey Techniques and Methods, book 6, chap. A43, 2013. https://doi.org/10.3133/tm6A43

[43] C.I. Steefel, C.A.J. Appelo, B. Arora, D. Jacques, T. Kalbacher, O. Kolditz, V. Lagneau, P.C. Lichtner, K.U. Mayer, J.C.L. Meeussen, S. Molins, D. Moulton, H. Shao, J. Šimůnek, N. Spycher, S.B. Yabusaki, G.T. Yeh, Reactive transport codes for subsurface environmental simulation, Comput. Geosci. 19 (2015) 445–478. https://doi.org/10.1007/s10596-014-9443-x

[44] E.S.P. Aradóttir, E.L. Sonnenthal, G. Björnsson, H. Jónsson, Multidimensional reactive transport modeling of CO_2 mineral sequestration in basalts at the Hellisheidi geothermal field, Iceland, Int. J. Greenh. Gas Control 9 (2012) 24–40. https://doi.org/10.1016/j.ijggc.2012.02.006

[45] E. Ranaee, Z. Karami Ziarani, F. Inzoli, Interplay between fracture network arrangement and efficiency of CO_2 mineralization in basaltic aquifers, Geoenergy 4 (2026). https://doi.org/10.1144/geoenergy2026-012

[46] A.C. Lasaga, Chemical kinetics of water–rock interactions, J. Geophys. Res. 89 (1984) 4009–4025. https://doi.org/10.1029/JB089iB06p04009

[47] J. Schott, O.S. Pokrovsky, E.H. Oelkers, The link between mineral dissolution/precipitation kinetics and solution chemistry, Rev. Mineral. Geochem. 70 (2009) 207–258. https://doi.org/10.1515/9781501508462-008

[48] J.L. Palandri, Y.K. Kharaka, A compilation of rate parameters of water–mineral interaction kinetics for application to geochemical modeling, U.S. Geological Survey Open File Report 2004-1068, 2004. https://doi.org/10.3133/ofr20041068

[49] J. Kozeny, Über kapillare Leitung des Wassers im Boden, Sitzungsber. Akad. Wiss. Wien 136 (1927) 271–306.

[50] P.C. Carman, Fluid flow through granular beds, Trans. Inst. Chem. Eng. 15 (1937) 150–166.

[51] J. Hommel, E. Coltman, H. Class, Porosity–permeability relations for evolving pore space: A review with a focus on (bio-)geochemically altered porous media, Transp. Porous Media 124 (2018) 589–629. https://doi.org/10.1007/s11242-018-1086-2

[52] C.A. Peters, Accessibilities of reactive minerals in consolidated sedimentary rock: An imaging study of three sandstones, Chem. Geol. 265 (2009) 198–208. https://doi.org/10.1016/j.chemgeo.2008.11.014

[53] G. Landrot, J.B. Ajo-Franklin, L. Yang, S. Cabrini, C.I. Steefel, Measurement of accessible reactive surface area in a sandstone, with application to CO_2 mineralization, Chem. Geol. 318–319 (2012) 113–125. https://doi.org/10.1016/j.chemgeo.2012.05.010

[54] L.E. Beckingham, E.H. Mitnick, C.I. Steefel, S. Zhang, M. Voltolini, A.M. Swift, L. Yang, D.R. Cole, J.M. Sheets, J.B. Ajo-Franklin, D.J. DePaolo, S. Mito, Z. Xue, Evaluation of mineral reactive surface area estimates for prediction of reactivity of a multi-mineral sediment, Geochim. Cosmochim. Acta 188 (2016) 310–329. https://doi.org/10.1016/j.gca.2016.05.040

[55] S. Molins, D. Trebotich, C.I. Steefel, C. Shen, An investigation of the effect of pore scale flow on average geochemical reaction rates using direct numerical simulation, Water Resour. Res. 48 (2012) W03527. https://doi.org/10.1029/2011WR011404

[56] L. Li, C.A. Peters, M.A. Celia, Upscaling geochemical reaction rates using pore-scale network modeling, Adv. Water Resour. 29 (2006) 1351–1370. https://doi.org/10.1016/j.advwatres.2005.10.011

[57] C. Noiriel, C. Soulaine, Pore-scale imaging and modelling of reactive flow in evolving porous media: Tracking the dynamics of the fluid–rock interface, Transp. Porous Media 140 (2021) 181–213. https://doi.org/10.1007/s11242-021-01613-2

[58] J. Simpson, M. Peč, H. O'Ghaffari, S.C. Mahavadi, J.E. Elkhoury, The effects of carbonate precipitation on the physical properties of basalt, AGU Adv. 7 (2026) e2025AV002110. https://doi.org/10.1029/2025AV002110

[59] A. Verma, K. Pruess, Thermohydrological conditions and silica redistribution near high-level nuclear wastes emplaced in saturated geological formations, J. Geophys. Res. 93 (1988) 1159–1173. https://doi.org/10.1029/JB093iB02p01159

[60] I. Galeczka, D. Wolff-Boenisch, E.H. Oelkers, S.R. Gislason, An experimental study of basaltic glass–H_2O–CO_2 interaction at 22 and 50 °C: Implications for subsurface storage of CO_2, Geochim. Cosmochim. Acta 126 (2014) 123–145. https://doi.org/10.1016/j.gca.2013.10.044

[61] S. Gudbrandsson, D. Wolff-Boenisch, S.R. Gislason, E.H. Oelkers, An experimental study of crystalline basalt dissolution from $2 \leq pH \leq 11$ and temperatures from 5 to 75 °C, Geochim. Cosmochim. Acta 75 (2011) 5496–5509. https://doi.org/10.1016/j.gca.2011.06.035

[62] S.R. Gislason, E.H. Oelkers, Mechanism, rates, and consequences of basaltic glass dissolution: II. An experimental study of the dissolution rates of basaltic glass as a function of pH and temperature, Geochim. Cosmochim. Acta 67 (2003) 3817–3832. https://doi.org/10.1016/S0016-7037(03)00176-5

[63] E.H. Oelkers, S.R. Gislason, The mechanism, rates and consequences of basaltic glass dissolution: I. An experimental study of the dissolution rates of basaltic glass as a function of aqueous Al, Si and oxalic acid concentration at 25 °C and pH = 3 and 11, Geochim. Cosmochim. Acta 65 (2001) 3671–3681. https://doi.org/10.1016/S0016-7037(01)00664-0

[64] O.S. Pokrovsky, J. Schott, Kinetics and mechanism of forsterite dissolution at 25 °C and pH from 1 to 12, Geochim. Cosmochim. Acta 64 (2000) 3313–3325. https://doi.org/10.1016/S0016-7037(00)00434-8

[65] D. Wolff-Boenisch, S. Wenau, S.R. Gislason, E.H. Oelkers, Dissolution of basalts and peridotite in seawater, in the presence of ligands, and CO_2: Implications for mineral sequestration of carbon dioxide, Geochim. Cosmochim. Acta 75 (2011) 5510–5525. https://doi.org/10.1016/j.gca.2011.07.004

[66] R. Hellmann, J.-M. Penisson, R.L. Hervig, J.-H. Thomassin, M.-F. Abrioux, An EFTEM/HRTEM high-resolution study of the near surface of labradorite feldspar altered at acid pH: Evidence for interfacial dissolution–reprecipitation, Phys. Chem. Miner. 30 (2003) 192–197. https://doi.org/10.1007/s00269-003-0308-4

[67] R. Hellmann, R. Wirth, D. Daval, J.-P. Barnes, J.-M. Penisson, D. Tisserand, T. Epicier, B. Florin, R.L. Hervig, Unifying natural and laboratory chemical weathering with interfacial dissolution–reprecipitation: A study based on the nanometer-scale chemistry of fluid–silicate interfaces, Chem. Geol. 294–295 (2012) 203–216. https://doi.org/10.1016/j.chemgeo.2011.12.002

[68] E. Ruiz-Agudo, C.V. Putnis, C. Rodriguez-Navarro, A. Putnis, Mechanism of leached layer formation during chemical weathering of silicate minerals, Geology 40 (2012) 947–950. https://doi.org/10.1130/G33339.1

[69] A. Putnis, Mineral replacement reactions, Rev. Mineral. Geochem. 70 (2009) 87–124. https://doi.org/10.2138/rmg.2009.70.3

[70] S.T. Mergelsberg, B.P. Rajan, B.A. Legg, L. Kovarik, S.D. Burton, G.M. Bowers, M.E. Bowden, O. Qafoku, C.J. Thompson, S.N. Kerisit, E.S. Ilton, J.S. Loring, Nanoscale Mg-depleted layers slow carbonation of forsterite (Mg_2SiO_4) when water is limited, Environ. Sci. Technol. Lett. 10 (2023) 98–104. https://doi.org/10.1021/acs.estlett.2c00866

[71] H.E. King, O. Plümper, A. Putnis, Effect of secondary phase formation on the carbonation of olivine, Environ. Sci. Technol. 44 (2010) 6503–6509. https://doi.org/10.1021/es9038193

[72] A.H. Menefee, P. Li, D.E. Giammar, B.R. Ellis, Roles of transport limitations and mineral heterogeneity in carbonation of fractured basalts, Environ. Sci. Technol. 51 (2017) 9352–9362. https://doi.org/10.1021/acs.est.7b00326

[73] A.P. Gysi, A. Stefánsson, CO_2–water–basalt interaction. Numerical simulation of low temperature CO_2 sequestration into basalts, Geochim. Cosmochim. Acta 75 (2011) 4728–4751. https://doi.org/10.1016/j.gca.2011.05.037

[74] A.P. Gysi, A. Stefánsson, CO_2–water–basalt interaction. Low temperature experiments and implications for CO_2 sequestration into basalts, Geochim. Cosmochim. Acta 81 (2012) 129–152. https://doi.org/10.1016/j.gca.2011.12.012

[75] D.E. Clark, I.M. Galeczka, K. Dideriksen, M.J. Voigt, D. Wolff-Boenisch, S.R. Gíslason, Experimental observations of CO_2–water–basaltic glass interaction in a large column reactor experiment at 50 °C, Int. J. Greenh. Gas Control 89 (2019) 9–19. https://doi.org/10.1016/j.ijggc.2019.07.007

[76] D. Wolff-Boenisch, I.M. Galeczka, Flow-through reactor experiments on basalt–(sea)water–CO_2 reactions at 90 °C and neutral pH. What happens to the basalt pore space under post-injection conditions?, Int. J. Greenh. Gas Control 68 (2018) 176–190. https://doi.org/10.1016/j.ijggc.2017.11.013

[77] A.H. Menefee, D.E. Giammar, B.R. Ellis, Permanent CO_2 trapping through localized and chemical gradient-driven basalt carbonation, Environ. Sci. Technol. 52 (2018) 8954–8964. https://doi.org/10.1021/acs.est.8b01814

[78] S. Peuble, M. Godard, L. Luquot, M. Andreani, I. Martinez, P. Gouze, CO_2 geological storage in olivine rich basaltic aquifers: New insights from reactive-percolation experiments, Appl. Geochem. 52 (2015) 174–190. https://doi.org/10.1016/j.apgeochem.2014.11.024

[79] D.A. Laird, Influence of layer charge on swelling of smectites, Appl. Clay Sci. 34 (2006) 74–87. https://doi.org/10.1016/j.clay.2006.01.009

[80] R.A. Robie, B.S. Hemingway, Thermodynamic properties of minerals and related substances at 298.15 K and 1 bar (10^5 pascals) pressure and at higher temperatures, U.S. Geological Survey Bulletin 2131, 1995. https://doi.org/10.3133/b2131

[81] M.A. Velbel, Formation of protective surface layers during silicate-mineral weathering under well-leached, oxidizing conditions, Am. Mineral. 78 (1993) 405–414.

[82] J.T. Adeoye, A.H. Menefee, W. Xiong, R.K. Wells, P. Skemer, D.E. Giammar, B.R. Ellis, Effect of transport limitations and fluid properties on reaction products in fractures of unaltered and serpentinized basalt exposed to high PCO_2 fluids, Int. J. Greenh. Gas Control 63 (2017) 310–320. https://doi.org/10.1016/j.ijggc.2017.06.003

[83] W. Xiong, R.K. Wells, A.H. Menefee, P. Skemer, B.R. Ellis, D.E. Giammar, CO_2 mineral trapping in fractured basalt, Int. J. Greenh. Gas Control 66 (2017) 204–217. https://doi.org/10.1016/j.ijggc.2017.10.003

[84] A. Putnis, G. Mauthe, The effect of pore size on cementation in porous rocks, Geofluids 1 (2001) 37–41. https://doi.org/10.1046/j.1468-8123.2001.11001.x

[85] S. Emmanuel, B. Berkowitz, Effects of pore-size controlled solubility on reactive transport in heterogeneous rock, Geophys. Res. Lett. 34 (2007) L06404. https://doi.org/10.1029/2006GL028962

[86] A.G. Stack, A. Fernandez-Martinez, L.F. Allard, J.L. Bañuelos, G. Rother, L.M. Anovitz, D.R. Cole, G.A. Waychunas, Pore-size-dependent calcium carbonate precipitation controlled by surface chemistry, Environ. Sci. Technol. 48 (2014) 6177–6183. https://doi.org/10.1021/es405574a

[87] M. Nooraiepour, M. Masoudi, H. Hellevang, Carbon mineralization in CO_2–seawater–basalt systems: Reactive transport dynamics and vesicular pore architecture controls, Langmuir 42 (2026) 11435–11456. https://doi.org/10.1021/acs.langmuir.6c00958

[88] G.J. Stockmann, D. Wolff-Boenisch, N. Bovet, S.R. Gislason, E.H. Oelkers, The role of silicate surfaces on calcite precipitation kinetics, Geochim. Cosmochim. Acta 135 (2014) 231–250. https://doi.org/10.1016/j.gca.2014.03.015

[89] G.J. Stockmann, D. Wolff-Boenisch, S.R. Gislason, E.H. Oelkers, Do carbonate precipitates affect dissolution kinetics? 1: Basaltic glass, Chem. Geol. 284 (2011) 306–316. https://doi.org/10.1016/j.chemgeo.2011.03.010

[90] G.J. Stockmann, D. Wolff-Boenisch, S.R. Gislason, E.H. Oelkers, Do carbonate precipitates affect dissolution kinetics? 2: Diopside, Chem. Geol. 337–338 (2013) 56–66. https://doi.org/10.1016/j.chemgeo.2012.11.014

[91] P.B. Kelemen, G. Hirth, Reaction-driven cracking during retrograde metamorphism: Olivine hydration and carbonation, Earth Planet. Sci. Lett. 345–348 (2012) 81–89. https://doi.org/10.1016/j.epsl.2012.06.018

[92] J.F. Rudge, P.B. Kelemen, M. Spiegelman, A simple model of reaction-induced cracking applied to serpentinization and carbonation of peridotite, Earth Planet. Sci. Lett. 291 (2010) 215–227. https://doi.org/10.1016/j.epsl.2010.01.016

[93] B. Jamtveit, A. Malthe-Sørenssen, O. Kostenko, Reaction enhanced permeability during retrogressive metamorphism, Earth Planet. Sci. Lett. 267 (2008) 620–627. https://doi.org/10.1016/j.epsl.2007.12.016

[94] W. Zhu, F. Fusseis, H. Lisabeth, T. Xing, X. Xiao, V. De Andrade, S. Karato, Experimental evidence of reaction-induced fracturing during olivine carbonation, Geophys. Res. Lett. 43 (2016) 9535–9543. https://doi.org/10.1002/2016GL070834

[95] T. Xing, W. Zhu, F. Fusseis, H. Lisabeth, Generating porosity during olivine carbonation via dissolution channels and expansion cracks, Solid Earth 9 (2018) 879–896. https://doi.org/10.5194/se-9-879-2018

[96] H.P. Lisabeth, W. Zhu, P.B. Kelemen, A. Ilgen, Experimental evidence for chemo-mechanical coupling during carbon mineralization in ultramafic rocks, Earth Planet. Sci. Lett. 474 (2017) 355–367. https://doi.org/10.1016/j.epsl.2017.06.045

[97] H.T. Schaef, B.P. McGrail, A.T. Owen, B.W. Arey, Mineralization of basalts in the CO_2–H_2O–H_2S system, Int. J. Greenh. Gas Control 16 (2013) 187–196. https://doi.org/10.1016/j.ijggc.2013.03.020

[98] C. Marieni, J. Přikryl, E.S. Aradóttir, I. Gunnarsson, A. Stefánsson, Towards 'green' geothermal energy: Co-mineralization of carbon and sulfur in geothermal reservoirs, Int. J. Greenh. Gas Control 77 (2018) 96–105. https://doi.org/10.1016/j.ijggc.2018.07.011

[99] H.T. Schaef, J.A. Horner, A.T. Owen, C.J. Thompson, J.S. Loring, B.P. McGrail, Mineralization of basalts in the CO_2–H_2O–SO_2–O_2 system, Environ. Sci. Technol. 48 (2014) 5298–5305. https://doi.org/10.1021/es404964j

[100] R.J. Rosenbauer, B. Thomas, J.L. Bischoff, J. Palandri, Carbon sequestration via reaction with basaltic rocks: Geochemical modeling and experimental results, Geochim. Cosmochim. Acta 89 (2012) 116–133. https://doi.org/10.1016/j.gca.2012.04.042

[101] G. Stockmann, D. Wolff-Boenisch, S.R. Gíslason, E.H. Oelkers, Dissolution of diopside and basaltic glass: The effect of carbonate coating, Mineral. Mag. 72 (2008) 135–139. https://doi.org/10.1180/minmag.2008.072.1.135

[102] J. Hövelmann, H. Austrheim, A. Beinlich, I.A. Munz, Experimental study of the carbonation of partially serpentinized and weathered peridotites, Geochim. Cosmochim. Acta 75 (2011) 6760–6779. https://doi.org/10.1016/j.gca.2011.08.032

[103] M. Andreani, L. Luquot, P. Gouze, M. Godard, E. Hoisé, B. Gibert, Experimental study of carbon sequestration reactions controlled by the percolation of CO_2-rich brine through peridotites, Environ. Sci. Technol. 43 (2009) 1226–1231. https://doi.org/10.1021/es8018429

[104] M. Voigt, C. Marieni, A. Baldermann, I.M. Galeczka, D. Wolff-Boenisch, E.H. Oelkers, S.R. Gislason, An experimental study of basalt–seawater–CO_2 interaction at 130 °C, Geochim. Cosmochim. Acta 308 (2021) 21–41. https://doi.org/10.1016/j.gca.2021.05.056

[105] S. Kanakiya, L. Adam, L. Esteban, M.C. Rowe, P. Shane, Dissolution and secondary mineral precipitation in basalts due to reactions with carbonic acid, J. Geophys. Res. Solid Earth 122 (2017) 4312–4327. https://doi.org/10.1002/2017JB014019

[106] L. Adam, K. van Wijk, T. Otheim, M. Batzle, Changes in elastic wave velocity and rock microstructure due to basalt–CO_2–water reactions, J. Geophys. Res. Solid Earth 118 (2013) 4039–4047. https://doi.org/10.1002/jgrb.50302

[107] H.T. Schaef, B.P. McGrail, A.T. Owen, Basalt–CO_2–H_2O interactions and variability in carbonate mineralization rates, Energy Procedia 1 (2009) 4899–4906. https://doi.org/10.1016/j.egypro.2009.02.320

[108] H.T. Schaef, B.P. McGrail, A.T. Owen, Basalt reactivity variability with reservoir depth in supercritical CO_2 and aqueous phases, Energy Procedia 4 (2011) 4977–4984. https://doi.org/10.1016/j.egypro.2011.02.468

[109] W. Xiong, R.K. Wells, J.A. Horner, H.T. Schaef, P.A. Skemer, D.E. Giammar, CO_2 mineral sequestration in naturally porous basalt, Environ. Sci. Technol. Lett. 5 (2018) 142–147. https://doi.org/10.1021/acs.estlett.8b00047

[110] A.J. Luhmann, B.M. Tutolo, B.C. Bagley, D.F. Mildner, W.E. Seyfried Jr., M.O. Saar, Permeability, porosity, and mineral surface area changes in basalt cores induced by reactive transport of CO_2-rich brine, Water Resour. Res. 53 (2017) 1908–1927. https://doi.org/10.1002/2016WR019216

[111] A.J. Luhmann, B.M. Tutolo, C. Tan, B.M. Moskowitz, M.O. Saar, W.E. Seyfried Jr., Whole rock basalt alteration from CO_2-rich brine during flow-through experiments at 150 °C and 150 bar, Chem. Geol. 453 (2017) 92–110. https://doi.org/10.1016/j.chemgeo.2017.02.002

[112] P. Shafabakhsh, B. Cordonnier, T. Le Borgne, J. Mathiesen, G. Linga, A. Pluymakers, A. Kaestner, A. Tengattini, F. Renard, Coupling neutron and X-ray imaging of fluid mixing and precipitation in rocks: Challenges and opportunities, Water Resour. Res. 61 (2025) e2025WR041911. https://doi.org/10.1029/2025WR041911

[113] M. Andreani, L. Luquot, P. Gouze, M. Godard, B. Gibert, Experimental carbonation of peridotite by percolation of CO_2-rich fluids, Geophys. Res. Abstr. 10 (2008) EGU2008-A-10042.

[114] G.D. Saldi, G. Jordan, J. Schott, E.H. Oelkers, Magnesite growth rates as a function of temperature and saturation state, Geochim. Cosmochim. Acta 73 (2009) 5646–5657. https://doi.org/10.1016/j.gca.2009.06.035

[115] G.D. Saldi, J. Schott, O.S. Pokrovsky, Q. Gautier, E.H. Oelkers, An experimental study of magnesite precipitation rates at neutral to alkaline conditions and 100–200 °C as a function of pH, aqueous solution composition and chemical affinity, Geochim. Cosmochim. Acta 83 (2012) 93–109. https://doi.org/10.1016/j.gca.2011.12.005

[116] C. Marieni, J.M. Matter, D.A.H. Teagle, Experimental study on mafic rock dissolution rates within CO_2–seawater–rock systems, Geochim. Cosmochim. Acta 272 (2020) 259–275. https://doi.org/10.1016/j.gca.2020.01.004

[117] A. Mukhametdinova, P. Mikhailova, E. Kozlova, T. Karamov, A. Baluev, A. Cheremisin, Effect of thermal exposure on oil shale saturation and reservoir properties, Appl. Sci. 10 (2020) 9065. https://doi.org/10.3390/app10249065

[118] A. Mukhametdinova, T. Karamov, S. Markovic, A. Morkovkin, A. Burukhin, E. Popov, Z.-Q. Sun, R.-B. Zhao, A. Cheremisin, Exploring in-situ combustion effects on reservoir properties of heavy oil carbonate reservoir, Pet. Sci. 21 (2024) 3363–3378. https://doi.org/10.1016/j.petsci.2024.04.014

[119] T.I. Karamov, E.Yu. Popov, A.I. Khairullina, M.Yu. Spasennykh, N.V. Lesina, A.A. Prokhorova, E.A. Bakumenko, A.N. Protsenko, A.A. Ryazanov, A.S. Ermakov, Technology-induced mineral formation in carbonate rocks-reservoirs of heavy hydrocarbons under laboratory high-temperature filtration experiments, Neftyanoe Khozyaystvo – Oil Industry (2024) 60–64.

[120] R. Fazlyeva, T. Karamov, M. Ursenbach, R. Aguilera, A. Voropaev, M. Spasennykh, G. Moore, A. Cheremisin, M. Sudarshan, In-situ combustion of heavy oil within a vuggy carbonate reservoir: Part II—Mechanism of permeability inversion and rock fabric transformation, Pet. Sci. 23 (2026) 3556–3575. https://doi.org/10.1016/j.petsci.2026.02.008

[121] R.G. Loucks, R.M. Reed, S.C. Ruppel, D.M. Jarvie, Morphology, genesis, and distribution of nanometer-scale pores in siliceous mudstones of the Mississippian Barnett Shale, J. Sediment. Res. 79 (2009) 848–861. https://doi.org/10.2110/jsr.2009.092

[122] G. Desbois, J.L. Urai, P.A. Kukla, Morphology of the pore space in claystones — evidence from BIB/FIB ion beam sectioning and cryo-SEM observations, eEarth 4 (2009) 15–22. https://doi.org/10.5194/ee-4-15-2009

[123] T. Karamov, E. Leushina, E. Kozlova, M. Spasennykh, Broad ion beam–scanning electron microscopy characterization of organic porosity evolution during thermal treatment of Bazhenov shale sample, SPE Reserv. Eval. Eng. 26 (2023) 64–74. https://doi.org/10.2118/210599-PA

[124] V. Cnudde, M.N. Boone, High-resolution X-ray computed tomography in geosciences: A review of the current technology and applications, Earth-Sci. Rev. 123 (2013) 1–17. https://doi.org/10.1016/j.earscirev.2013.04.003

[125] D. Wildenschild, A.P. Sheppard, X-ray imaging and analysis techniques for quantifying pore-scale structure and processes in subsurface porous medium systems, Adv. Water Resour. 51 (2013) 217–246. https://doi.org/10.1016/j.advwatres.2012.07.018

[126] C. Noiriel, Resolving time-dependent evolution of pore-scale structure, permeability and reactivity using X-ray microtomography, Rev. Mineral. Geochem. 80 (2015) 247–286. https://doi.org/10.1515/9781501502071-008

[127] H.P. Menke, B. Bijeljic, M.G. Andrew, M.J. Blunt, Dynamic three-dimensional pore-scale imaging of reaction in a carbonate at reservoir conditions, Environ. Sci. Technol. 49 (2015) 4407–4414. https://doi.org/10.1021/es505789f

[128] P.J. Heaney, E.P. Vicenzi, L.A. Giannuzzi, K.J.T. Livi, Focused ion beam milling: A method of site-specific sample extraction for microanalysis of Earth and planetary materials, Am. Mineral. 86 (2001) 1094–1099. https://doi.org/10.2138/am-2001-8-917

[129] R. Wirth, Focused Ion Beam (FIB) combined with SEM and TEM: Advanced analytical tools for studies of chemical composition, microstructure and crystal structure in geomaterials on a nanometre scale, Chem. Geol. 261 (2009) 217–229. https://doi.org/10.1016/j.chemgeo.2008.05.019

[130] M.E. Curtis, C.H. Sondergeld, R.J. Ambrose, C.S. Rai, Microstructural investigation of gas shales in two and three dimensions using nanometer-scale resolution imaging, AAPG Bull. 96 (2012) 665–677. https://doi.org/10.1306/08151110188

[131] L.M. Keller, P. Schuetz, R. Erni, M.D. Rossell, F. Lucas, P. Gasser, L. Holzer, Characterization of multi-scale microstructural features in Opalinus Clay, Microporous Mesoporous Mater. 170 (2013) 83–94. https://doi.org/10.1016/j.micromeso.2012.11.029

[132] M.J. Blunt, B. Bijeljic, H. Dong, O. Gharbi, S. Iglauer, P. Mostaghimi, A. Paluszny, C. Pentland, Pore-scale imaging and modelling, Adv. Water Resour. 51 (2013) 197–216. https://doi.org/10.1016/j.advwatres.2012.03.003

[133] H. Andrä, N. Combaret, J. Dvorkin, E. Glatt, J. Han, M. Kabel, Y. Keehm, F. Krzikalla, M. Lee, C. Madonna, M. Marsh, T. Mukerji, E.H. Saenger, R. Sain, N. Saxena, S. Ricker, A. Wiegmann, X. Zhan, Digital rock physics benchmarks — Part I: Imaging and segmentation, Comput. Geosci. 50 (2013) 25–32. https://doi.org/10.1016/j.cageo.2012.09.005

[134] C. Noiriel, D. Daval, Pore-scale geochemical reactivity associated with CO_2 storage: New frontiers at the fluid–solid interface, Acc. Chem. Res. 50 (2017) 759–768. https://doi.org/10.1021/acs.accounts.7b00019

[135] T. Karamov, V. White, E. Idrisova, E. Kozlova, A. Burukhin, A. Morkovkin, M. Spasennykh, Alterations of carbonate mineral matrix and kerogen micro-structure in Domanik organic-rich shale during anhydrous pyrolysis, Minerals 12 (2022) 870. https://doi.org/10.3390/min12070870